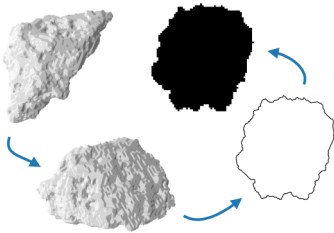


Graphical Abstract

Simulated Particle Imaging Dataset for Correlations of 2D and 3D Particle Properties

Thomas Buchwald, Ralf Ditscherlein, Urs A. Peuker



Highlights

Simulated Particle Imaging Dataset for Correlations of 2D and 3D Particle Properties

Thomas Buchwald, Ralf Ditscherlein, Urs A. Peuker

- Workflow for simulation of static and dynamic image analysis is presented.
- Particle characteristics for several solids types are determined.
- Influence of image analysis methods on shape factors are shown.
- A correlation for 3D sphericity from 2D shape factors is derived.

Simulated Particle Imaging Dataset for Correlations of 2D and 3D Particle Properties

Thomas Buchwald, Ralf Ditscherlein, Urs A. Peuker

*Institute of Mechanical Process Engineering and Mineral Processing, TU Bergakademie
Freiberg, Agricolastr. 1, 09599, Freiberg, Germany*

Abstract

Particle size and shape characteristics are commonly measured with two-dimensional (2D) imaging techniques, two of which are static or dynamic imaging techniques. These 2D particle characteristics need to be applied to particulate processes where they model three-dimensional (3D) processes. The correlation between 2D and 3D particle characteristics is therefore necessary, but the knowledge is still limited to either mathematically simple shapes or specific sets of investigated bulk solids.

A particle dataset consisting of six bulk solids measured with X-ray microscopy was used to simulate the results of 2D imaging techniques to create a database to test the correlation between sets of particle characteristics. The dataset thus created offers the possibility to study the correlation between characteristic values and robustly predict the 3D properties of bulk solids measured with 2D measurement techniques. Several correlations are determined, including between circularity (2D) and sphericity (3D), and Feret diameters (2D) and particle width (3D).

Keywords: imaging techniques, static image analysis, dynamic image analysis, circularity, sphericity, shape factors, equivalent particle size, particle characteristics, correlation

1. Introduction

The characterization of particles regarding size and shape is essential for most particulate processes. Advances in measuring techniques have made the tomographic measurement of bulk solids and resulting particle-discrete datasets possible, enabling new methods of analyzing, e.g., separation processes [1, 2].

However, tomographic measurement is a time-consuming and costly process, so the characterization of bulk solids in everyday industrial and laboratory applications is mostly done with other well-established techniques. For the measurement of particle size and shape in orders of magnitude from $1\ \mu\text{m}$ to $10\ \text{mm}$, static and dynamic image analysis are widely used, and have often replaced traditional sieve analysis [3, 4, 5]. Furthermore, inline particle measurements are becoming more abundant in research and industry [6, 7].

Wadell introduced the concept of sphericity to account for a particle sedimentation velocity deviating from the sedimentation velocity of a sphere [8, 9]. It has since been used by many researchers and practitioners to represent particle shape as a single value. But Wadell recognized that the true sphericity for single particles might be hard to come by – it was even deemed unmeasurable by peers [10] – so he proposed the measurement of the projection of a particle at rest and an alternative definition for sphericity from it (Eq. 14).

The classical approach by Zingg to classify particles into shape categories by the ratios of their principal dimensions (elongation and flatness) is still widely in use and has been recently implemented in a particle shape analysis tool [11, 12]. 2D aspect ratios, along with circularity and convexity, are recognized in the literature as meaningful shape descriptors [13].

Since Wadell, many people have investigated how 2D imaging techniques may accurately describe the “true”, 3D particle shape [14, 15, 16, 17, 18, 19]. In many ways, this study tries to retrace the steps of Bagheri et al. [20], who compared computed tomography measurements with projection images to find correlations to accurately describe 3D shape. Whereas before a particle’s three principal dimensions (length, width, and thickness) were defined as perpendicular to each other, with length being the dimension between the two points on the particle furthest from each other, the authors propose the determination from the two projections with minimum (for thickness) and maximum areas (for width and thickness). Their

38 results are interesting, while lacking statistical robustness because of the
39 small sample size.

40 To try to overcome the time-consuming task of measuring particle with
41 computed tomography, several researchers have shown how to simulate
42 realistic 3D particle data. Their work utilizes random fields [21] and spher-
43 ical harmonics [22]. Additional work has been done on reconstructing 3D
44 particles from 2D projections using convolutional neural networks [23, 24].
45 This happens in recognition of the approach of capturing single particles
46 from multiple angles to describe the 3D particle shape [25, 26]. The other
47 approach is to quantify particle shape accurately only in the statistical sense
48 by measuring enough particles to have a good estimate of the mean particle
49 shape of a given bulk solid [13].

50 In this study, we take the second approach by asking how well 2D
51 descriptors can describe 3D particle shape. The text comprises two distinct
52 parts. The first part is concerned with an expansive dataset of 3D particles
53 provided by the PARROT particle database¹ [27] and the simulation of
54 both static and dynamic image analysis. The resulting dataset is publicly
55 available (see Supplementary Data) and it is our hope that it can serve
56 as a foundation for investigation of many effects that accompany image
57 analysis and that have yet to be properly quantified. The second part tries
58 to correlate some 3D properties with 2D properties determined from the
59 simulated particle projections. This part of the study, sections 4.1 through
60 4.3, is meant to prove how meaningful the developed dataset is.

61 2. Materials and Methods

62 2.1. Particle Characteristics

63 The term *particle characteristic* as used in this text includes all parameters
64 that can describe the size and shape of a particle. It comprises three sub-
65 groups: *geometric properties*, *equivalent diameters* and *shape factors*. Geometric
66 properties can be directly measured from the 2D or 3D representation of
67 a given particle. Equivalent diameters are typically diameters of the circle
68 (2D) or sphere (3D) that share one of the geometrical properties of the par-
69 ticle. Finally, shape factors are mostly ratios of two different geometrical
70 properties, one of which may be calculated from the particle’s convex hull.

¹parrot.tu-freiberg.de

71 2.1.1. 2D Measures

72 These geometric properties can all be derived directly from the projec-
 73 tion or section of a particle in any direction (Fig. 1b); therefore, they are
 74 applicable to all 2D imaging techniques, like static and dynamic image
 75 analysis.

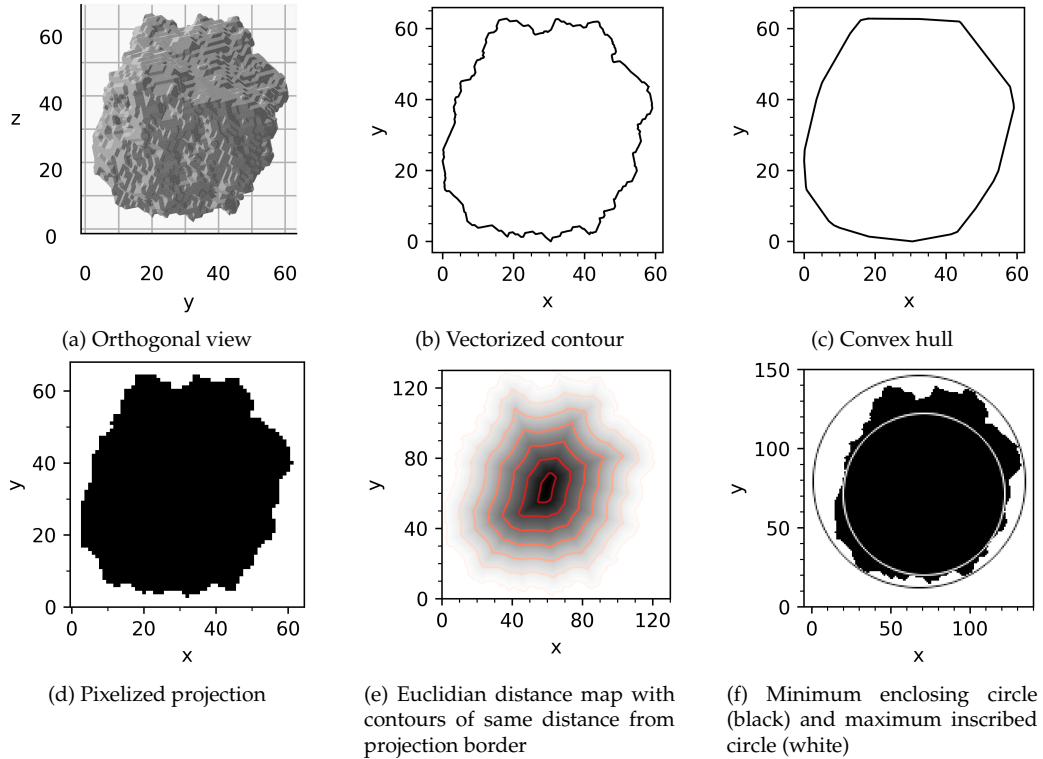


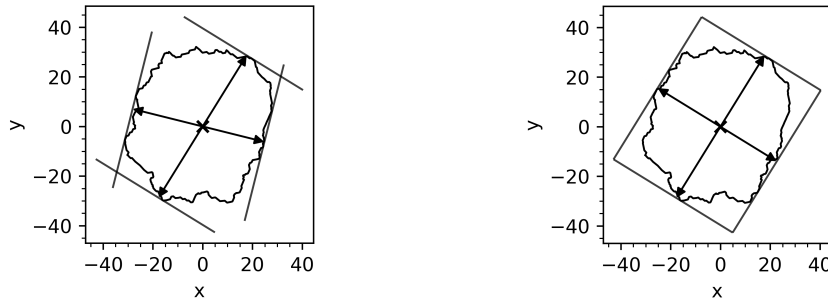
Figure 1: Illustration of methods for generation of 2D descriptors for particle shape

76 In the current study, only the vector representation of the silhouette
 77 image is used. The accuracy of the calculated parameters therefore only
 78 depends on the resolution of the original 3D surface mesh and the marching
 79 cubes procedure with which it was produced from the voxel representa-
 80 tions that themselves originated in the reconstructed tomography image
 81 stack. The contour is voxelized solely to simplify the calculation of bound-
 82 ing circles, enabling the use of standard Python libraries. Both pixeliza-
 83 tion and orthogonal projection images, as shown in Fig. 1a, offer possibili-
 84 ties for testing the effects of image resolution and roughness measurement,
 85 respectively.

86 *Area and perimeter.* Both the projection area A_p and the perimeter P_p are
 87 calculated by methods provided by the Shapely package, directly from the
 88 projection contour, as shown in Fig. 1b. Because of the inherent fractal
 89 behavior of many real solids' surfaces, the perimeter is much less robust
 90 than the projection area for smaller particles. Still, the effect of measure-
 91 ment resolution will be more pronounced in the determination of the (3D)
 92 surface area, where surface roughness comes more into effect than in the
 93 2D case [28].

94 *Convex Hull.* The convex hull is determined using a method of the Shapely
 95 polygon object that contains the contour. For the convex hull, both area A_c
 96 and perimeter P_c are determined.

97 *Feret Diameters.* Minimum and maximum Feret diameters are determined
 98 by brute force: the projection contour is rotated in 500 steps between
 99 0° and 180° , and the boundaries in both axis directions are determined.
 100 The smallest measured distance between boundaries will be the minimum
 101 Feret diameter $x_{Fe,min}$, while the largest distance will be the maximum
 102 Feret diameter $x_{Fe,max}$. The two measures, $x_{Fe,min}$ and $x_{Fe,max}$, are shown
 103 in Fig. 2a. As can be seen, the two Feret diameters are not necessarily at
 104 a right angle, which is why two *additional* Feret diameters are determined:
 105 $x_{Fe,min90}$ and $x_{Fe,max90}$, which are perpendicular to the $x_{Fe,max}$ and $x_{Fe,min}$,
 106 respectively.



(a) Maximum $x_{Fe,max}$ and minimum $x_{Fe,min}$ Feret diameters

(b) Maximum $x_{Fe,max}$ and perpendicular $x_{Fe,min90}$ Feret diameters

Figure 2: Illustration of of different definitions of Feret diameters

107 The use of perpendicular Feret diameters serves two purposes. Firstly,
 108 for static image analysis, the maximum and minimum Feret diameters will

109 be very close to the length and width of a particle, respectively (Fig. 2b).
110 Secondly, the (true) minimum Feret diameter $x_{\text{Fe},\text{min}}$ and its perpendicular
111 Feret diameter $x_{\text{Fe},\text{max}90}$ will, in most cases, be very close to the actual
112 dimensions of the oriented bounding box, i.e., the bounding box of least
113 area.

114 *Minimum Enclosing Circle.* The diameter of the minimum enclosing circle
115 d_{ec} belongs to the circle that has the least area while still containing the
116 entire projection contour (Fig. 1f). While dedicated Python packages for
117 the task of determining this measure exist, such as `miniball`, here, the
118 computer vision library `OpenCV` was used [29].

119 For the calculation of d_{ec} , the contour needs to be transformed into an
120 array first, equivalent to a pixel representation (Fig. 1d). The pixelization
121 is achieved with `scikit-image`, which contains the `polygon` method that
122 generates pixel coordinates inside a given polygon.

123 To increase the accuracy of d_{ec} (and d_{ic}), the contour coordinates are
124 scaled up by a factor of 2 before pixelization, significantly affecting on
125 the results of both the center coordinate of the circle as well as its radius.
126 Further scale-up is not considered necessary, or even useful, because the
127 original 3D mesh does not offer more resolution anyway.

128 *Maximum Inscribed Circle.* The determination of the maximum inscribed
129 circle d_{ic} for a 2D contour, as well as the maximum inscribed circle for a
130 3D surface, is not straightforward. For the authors, none of the methods
131 found in literature were computationally efficient and more robust than a
132 simple brute-force bisection algorithm.

133 A solution to efficiently determine the maximum inscribed circle was
134 found by discretization of the contour, i.e., pixelization. The method uses
135 the Euclidean distance transform as implemented in `scipy` [30]. The trans-
136 form calculates the distance of each object pixel from the background
137 (Fig. 1e). The pixel that contains the highest value after the transform will
138 be the center of the maximum inscribed circle, while the corresponding
139 pixel value will be $d_{\text{ic}}/2$, i.e., the radius of the circle. The Euclidean dis-
140 tance transform is computationally inexpensive and is a relatively simple
141 method for determining the maximum inscribed circle, as it transforms the
142 problem from vector space to pixel space. This reduces the complexity of
143 the problem significantly, albeit at the cost of being only as accurate as the
144 pixel dimensions allow.

145 It has since been found that the method described here has been used
146 in other particle-related research [31, 32].

147 2.1.2. 3D Measures

148 *Volume and Surface Area.* Both volume and surface area are properties of the
149 `trimesh` object that contains the particle mesh, so it is defined by functions
150 already implemented by the package.

151 However, using the surface area of the computed mesh leads to an error
152 in the determination of Wadell’s sphericity (cf. Eq. 8), where a maximum
153 value of $\psi_{\text{Wa}} \approx 0.92$ is reached even for highly spherical particles like
154 soda-lime glass.

155 An alternative determination of surface area is achieved with the collec-
156 tion of plugins `MorphoLibJ` for `ImageJ` [33]. From it, the `ParticleAnalysis3D`
157 plugin is used which computes the surface area of a 3D object with an N-
158 dimensional extension of the Crofton formula [34, 35]. Note that the origi-
159 nal Java libraries were used, accessed directly in Python through `Pyjnius`.
160 The accuracy of the method was tested by producing incrementally larger
161 spheres in discrete voxel representations and meshing them, using both
162 voxel representation and mesh for the calculation of surface area and par-
163 ticle volume. The result is shown in Fig. 3, where Wadell’s sphericity
164 has been calculated using all three permutations of equivalent diameters
165 calculated from two volume (x_V , Eq. 2) and two surface area (x_S , Eq. 3) def-
166 initions: $x_{V,\text{voxel}}$ uses the volume equal to the number of voxels, $x_{V,\text{mesh}}$ the
167 volume contained in the mesh produced by the marching cubes algorithm,
168 $x_{S,\text{crofton}}$ the approximation of surface area with the 3D Crofton formula,
169 and $x_{S,\text{mesh}}$ the surface area of the mesh directly.

170 It can be seen that using volume and surface area of the mesh leads
171 to a final sphericity value $\psi_{\text{Wa}} < 1$, even for spheres of diameters larger
172 than a hundred voxels. Using the information of the voxel representation
173 directly, as used in `MorphoLibJ` will result in sphericity values $\psi_{\text{Wa}} > 1$ for
174 smaller spheres, which is also counterintuitive. The underlying problem
175 is that not every voxel must be fully filled by the particle and the volume
176 approximated by counting the voxels is therefore too high. If the volume
177 of the mesh is used instead of the volume of the voxelized particle, i.e.,
178 $x_{V,\text{mesh}}$ instead of $x_{V,\text{voxel}}$, the resulting sphericity values will approach the
179 limit of $\psi_{\text{Wa}} \rightarrow 1$, with small spheres observing sphericity values $\psi_{\text{Wa}} < 1$.
180 As this definition of sphericity, as shown by the green points in Fig. 3a, is
181 the most intuitive and realistic one, the following strategy for 3D particle

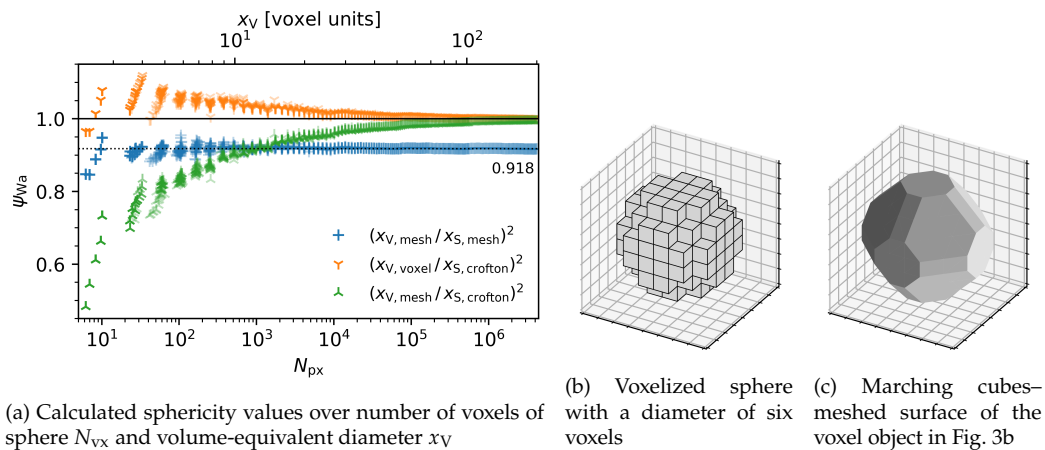


Figure 3: Sphericity values for different definitions of particle surface area and volume, illustration of marching cubes meshing result

182 property determination is recommended and used in this study:

- 183 • particle volume V_p is determined directly from the particle mesh,
- 184 • particle surface area S_p is determined with the 3D Crofton formula as
- 185 implemented in MorphoLibJ. For this, the particle mesh is voxelized
- 186 again.

187 *Specific Surface Area.* A combination of volume and area, specific surface

188 area is an important measure for all sorts of processes involving heat,

189 moment, or mass transfer. It is defined as:

$$S_V = \frac{S_p}{V_p} \quad (1)$$

190 In contrast to most other particle properties, specific surface area will

191 decrease with increasing particle volume. As explained above, the surface

192 area S_p is calculated from the voxelized surface, while the particle volume

193 V_p is computed from the meshed surface.

194 *Convex Hull.* The convex hull is another property of the trimesh object,

195 from which both volume V_c and surface area S_c can be calculated.

196 *Aligned Bounding Box.* In this study, a bounding box defines the main di-
197 mensions of the particle. The aligned bounding box defines the length l ,
198 width w , and thickness t to be the longest, intermediate, and shortest edge
199 lengths. This approach is congruent with the definition of particle dimen-
200 sions by Krumbein, who measured orthogonal lengths starting with the
201 longest one found on the particle [36], which is equivalent to the maximum
202 Feret diameter.

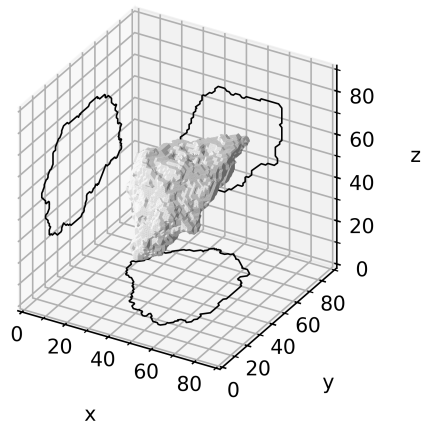
203 The aligned bounding box is created by transformation of the particle so
204 that its principal axes of inertia align with the cartesian dimension vectors
205 (Fig. 4b). The necessary transform is again a property of the `trimesh` object
206 containing the particle mesh. After the transformation, the bounding box,
207 again, is a property of the `trimesh` object (Fig. 4d).

208 The definition of 3D particle dimensions in this way also makes it
209 possible to directly compare measurements with static image analysis sim-
210 ulation results. When the maximum Feret $x_{\text{Fe,max}}$ and the perpendicular
211 Feret diameter $x_{\text{Fe,min}90}$ (Fig. 2b) are used, they will be identical with length
212 l and width w for the aligned particle (section 3.1). For stable positions,
213 section 3.2, $x_{\text{Fe,max}}$ should still reflect actual particle length l , while $x_{\text{Fe,min}90}$
214 should differ somewhat because the true particle width is oriented at an
215 angle to the projection direction, i.e., surface normal.

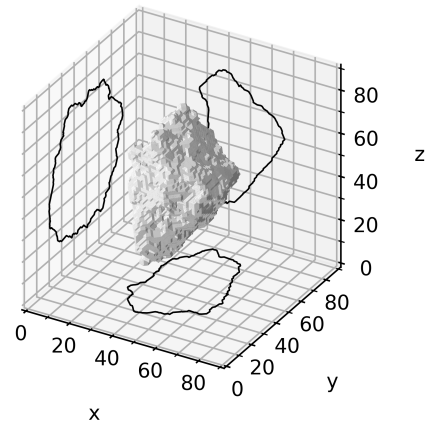
216 Bagheri et al. favoured the use of uncorrelated Feret extrema for the de-
217 termination of particle dimensions to reduce operator error [20]. However,
218 with most modern measurement setups particle dimensions are seldom
219 determined manually, and determination of a minimum Feret diameter
220 for compact projections may still be difficult if done manually anyway.

221 *Oriented Bounding Box.* The oriented bounding box is again calculated by
222 `trimesh` for a given particle mesh and represents the bounding box of least
223 volume that still contains the whole mesh surface (Fig. 4c). The dimensions
224 of the oriented bounding box are determined from the Cartesian coordi-
225 nates after applying the inverse transform on the bounding box, since the
226 oriented bounding box is likely to be at random angles toward the Cartesian
227 axes, even if the particle was first aligned to its principal axes of inertia.

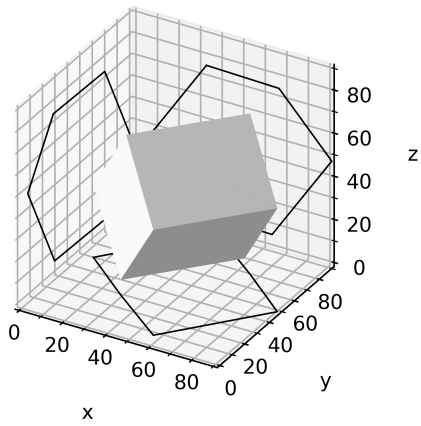
228 Fig. 5 shows comparisons of the dimensions of aligned bounding boxes
229 and oriented bounding boxes for all investigated particles. The oriented
230 bounding box has on average smaller dimensions than the aligned bound-
231 ing box. The effect increases for the longer dimensions: length will mostly
232 be smaller for the oriented bounding box, whereas there is a more random



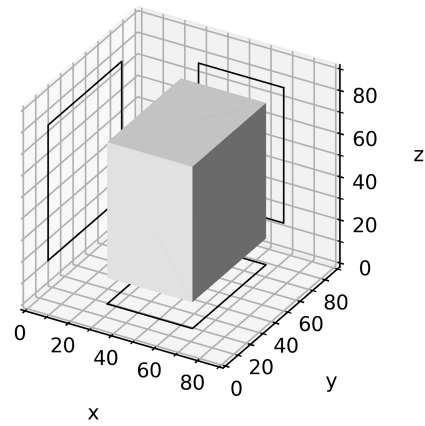
(a) 3D particle in its original position



(b) 3D particle of 4a after applying the principal axis alignment transform



(c) Oriented bounding box for particle in 4a, $V = 121\,486$



(d) Bounding box along Cartesian axes for aligned particle in 4b, $V = 146\,740$

Figure 4: Illustration of the two different definitions for bounding boxes, volumes given in axis units

233 scatter for thickness.

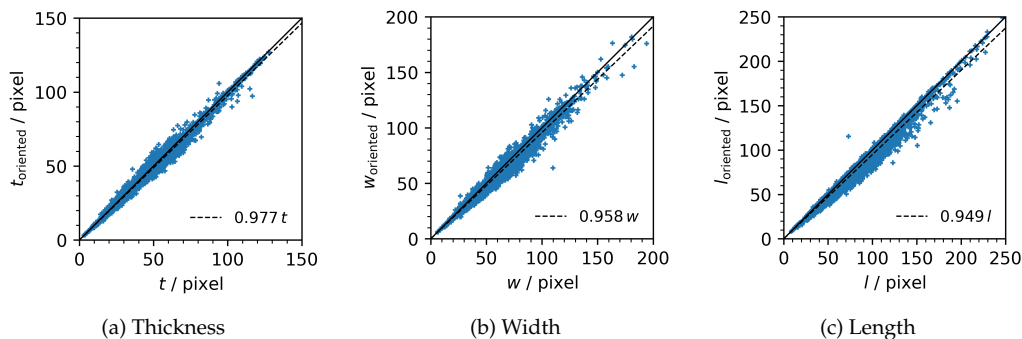


Figure 5: Comparison of dimensions determined by aligned and oriented bounding boxes

234 On average, the oriented bounding box will be 14 % smaller than the
235 aligned bounding box for compact particles. In contrast, the oriented
236 bounding box will only be 12 % smaller for mica particles which, because
237 of their flat nature, should, in their aligned position, already be closer to
238 the smallest box possible. Finally, soda-lime glass spheres have on average
239 oriented bounding boxes that are only 5.5 % smaller.

240 The aligned bounding box is preferred here over the oriented bounding
241 box because of its congruence with Krumbein’s definition who chose it
242 because it is easier to understand and determine by the practitioner.

243 *Bounding Spheres.* The minimum bounding sphere again is a property of
244 the mesh object defined by the `trimesh` library, so the diameter of the
245 minimum enclosing sphere d_{es} is determined in a single line of code. A
246 visualization of both bounding spheres is found in Fig. 6.

247 The maximum inscribed sphere is approximated as the maximum in-
248 scribed circle in the 2D case. In both cases, the function `distance_transform_edt`
249 from the `scipy` library [30] is used to calculate the Euclidean distance
250 transform to find the pixel/voxel that is furthest from the particle sur-
251 face. This maximum value will be the diameter of the maximum inscribed
252 sphere d_{is} .

253 In order to perform the Euclidean distance transform, the surface mesh
254 needs to be discretized into a voxel representation (Fig. 6c). The voxeliza-
255 tion is also done with methods provided by `trimesh`, and, as with the
256 2D case, at a scale factor of 2, which increases the accuracy of the diame-
257 ter estimation significantly. Care must be taken to produce a filled voxel

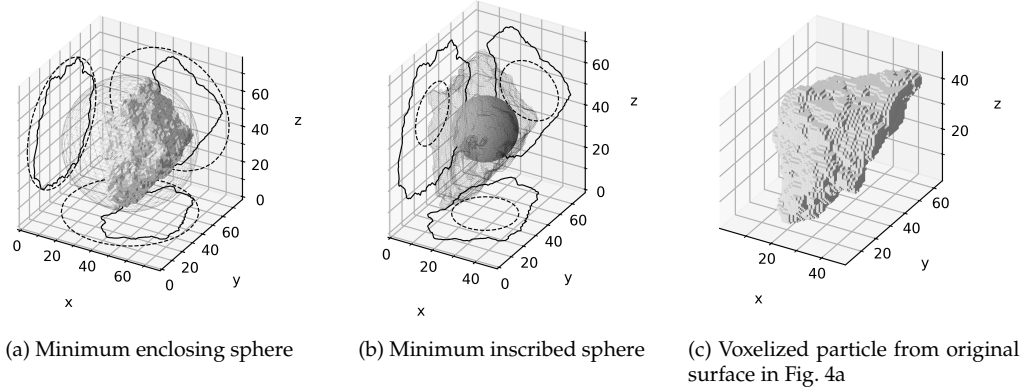


Figure 6: Illustration of both minimum enclosing sphere and maximum inscribed sphere

258 representation: most voxelization algorithms will only return solid voxels
 259 where the surface of the mesh touches. An extra step is involved to fill the
 260 hollow discretized surface with `scipy's` method `binary_fill_holes`.

261 2.1.3. Equivalent Diameters

262 Several properties in 2D and 3D can be compared to that of the idealized
 263 shapes, a circle in two and a sphere in three dimensions. In 3D, the diameter
 264 of a sphere can be calculated that has the same volume V_p as that of the
 265 particle. This diameter will be called the volume-equivalent diameter:

$$x_V = \sqrt[3]{\frac{6V_p}{\pi}} \quad (2)$$

266 In the same sense, the diameter of the sphere that has the same surface
 267 area S_p as that of the particle (surface-equivalent diameter) is:

$$x_S = \sqrt{\frac{S_p}{\pi}} \quad (3)$$

268 In two dimensions, the particle properties volume V_p and surface
 269 area S_p reduce to projection properties, projection area A_p and perimeter P_p .
 270 The diameter of the circle that has the same area as the projection area, the
 271 area-equivalent diameter, is:

$$x_A = \sqrt{\frac{4A_p}{\pi}} \quad (4)$$

272 Lastly, the perimeter-equivalent diameter is the diameter of the circle
273 that has the same perimeter as that of the particle projection, defined as:

$$x_P = \frac{P_P}{\pi} \quad (5)$$

274 2.1.4. Shape Factors

275 Shape factors are derived from two or three of the particle properties or
276 equivalent diameters introduced above. All shape factors described below
277 are dimensionless, which means they can be used to good effect to find
278 correlations between 2D projections and 3D particle properties.

279 *Length Ratios.* Flatness t/w and elongation w/l have been used before in
280 Fig. 8d to classify particles into shape categories.

281 In 2D, two more length ratios are used in this study. First the aspect
282 ratio is defined as the ratio of minimum and maximum Feret diameter:

$$AR = \frac{x_{Fe,min}}{x_{Fe,max}} \quad (6)$$

283 As discussed before, the two Feret diameters often at an angle $\neq 90^\circ$.
284 Because the 3D particle dimensions are defined by their bounding boxes,
285 they are necessarily at a right angle to each other. It therefore makes sense
286 to define an additional, orthogonal aspect ratio of perpendicular Feret
287 diameters:

$$AR_{90} = \frac{x_{Fe,min90}}{x_{Fe,max}} \quad (7)$$

288 *Sphericity.* Several sphericity definitions exist, some of them fundamentally
289 different from each other, but for all of them, the sphericity $\psi < 1$ for
290 particles deviating from a sphere.

291 The original definition of sphericity comes from Wadell for application
292 on sedimentary particles [8]. Wadell defined sphericity as the ratio of the
293 surface area of a sphere of equal volume as that of the particle to the actual
294 surface area of the particle:

$$\psi_{Wa} = \frac{S_{sp}}{S_p} = \left(\frac{x_V}{x_S} \right)^2 \quad (8)$$

295 S_{sp} is the surface area of the sphere having the same volume as the
296 particle.

297 Another sphericity definition is the ratio of the diameters of the two
 298 bounding spheres, i.e., maximum inscribed sphere to minimum enclosing
 299 sphere [37]:

$$\psi_{\text{bs}} = \frac{d_{\text{is}}}{d_{\text{es}}} \quad (9)$$

300 Hofmann applies the concept of statistical entropy to the particle shape
 301 description [38]:

$$\psi_{\text{Ho}} = \frac{1}{\ln(1/3)} \sum_{i=1}^3 p_i \ln p_i, \quad (10)$$

302 where $p_i = \frac{d_i}{d_1+d_2+d_3}$, $d_1 = l$, $d_2 = w$, and $d_3 = t$.

303 Hofmann's sphericity is supposed to be the most representative mea-
 304 sure for the prediction of particle settling velocity [39].

305 Lastly, Krumbein defined a sphericity by comparing a given particle to
 306 a triaxial ellipsoid [36]. After determining the longest dimension of the
 307 particle, the second longest dimension *perpendicular* to the first is deter-
 308 mined, with the third dimension being perpendicular to the other two.
 309 In this sense, the three dimensions are equivalent to length l , width w ,
 310 and thickness t of the bounding box of the principally aligned particle, as
 311 described in section 2.1.2.

$$\psi_{\text{Kr}} = \sqrt[3]{\frac{wt}{l^2}} \quad (11)$$

312 Another definition for sphericity has been defined by Sneed and Folk
 313 as $\psi_{\text{SF}} = \sqrt[3]{t^2/(wl)}$ [40], but will not be used in this study.

314 *Circularity*. "Circularity" is the name chosen according to the definitions
 315 of Wadell [9] for the 2D equivalent of sphericity, basically a "projection
 316 sphericity", sometimes also called "roundness" [41]. Like sphericity, circu-
 317 larity approaches a value of one for particles that closely resemble circular
 318 shapes and will decrease in value for particles becoming less compact.

319 The original circularity definition as ratio of perimeter of the area-
 320 equivalent circle to the actual projection perimeter is due to Wadell [9].
 321 Wadell stressed that circularity and sphericity are fundamentally differ-
 322 ent from roundness in the sense that roundness is a mesoscopic measure
 323 and circularity is a macroscopic measure. In other words, circularity and

324 sphericity show *shape* deviations, whereas roundness shows *surface* devia-
 325 tions.

$$\psi_c = \frac{P_c}{P_p} = \frac{x_A}{x_P} = \sqrt{\frac{4\pi A_p}{P_p^2}} \quad (12)$$

326 The square of circularity ψ_c is called the form factor and is equivalent
 327 to the “roundness” factor defined by Cox [42, 43, 44].

$$\text{FF} = \frac{4\pi A_p}{P_p^2} \quad (13)$$

328 Because one early criticism of ψ_{Wa} was the difficulty of measurement,
 329 Wadell proposed more easily attainable circularity measure:

$$\psi_{c,\text{Wa}} = \frac{x_{A,\text{stable}}}{d_{\text{ec}}} \quad (14)$$

330 In the above equation, $x_{A,\text{stable}}$ is the diameter of a circle of equal projec-
 331 tion area as that of a given particle *at rest*, i.e., lying on a surface in a stable
 332 position. d_{ec} is, as per previous definition, the diameter of the minimum
 333 enclosing circle.

334 Another method of defining circularity is through both bounding cir-
 335 cles, i.e., the radius of the maximum inscribed circle d_{ic} and the radius of
 336 the minimum enclosing circle d_{ec} :

$$\psi_{c,\text{bc}} = \frac{d_{\text{ic}}}{d_{\text{ec}}} \quad (15)$$

337 Eq. 15 is the square of the circularity definition by Riley [41].

338 *Solidity.* As a measure of concavity, a solidity factor S_x can be calculated in
 339 both 2D and 3D. It compares the actual particle volume or projection area
 340 to its convex hulls. If there are no concavities, the solidity will be 1 and the
 341 particle or projection will be its own convex hull.

$$S_{x,3\text{D}} = \frac{V_p}{V_c} \quad (16)$$

$$S_{x,2\text{D}} = \frac{A_p}{A_c} \quad (17)$$

342 *Convexity.* Another measure for deviation from a convex object is the con-
343 vexity, for which the symbol C_x is used. It compares the surface of particle
344 or projection directly to the convex hull.

$$C_{x,3D} = \frac{S_c}{S_p} \quad (18)$$

$$C_{x,2D} = \frac{P_c}{P_p} \quad (19)$$

345 2.2. Particle Datasets

346 2.2.1. Acquisition

347 The solids particle data used in this study was prepared previously for
348 the stated purpose of providing reference 3D datasets. A methodology was
349 developed to produce isolated, i.e., non-touching, particles in a wax matrix
350 [45, 46]. Tomographic reconstruction of X-ray microscopy measurements
351 of these wax matrices offers the possibility to easily segment and extract the
352 single 3D particles. The particle data is available in the form of the original
353 reconstructed tomography stacks as well as single particle surfaces in STL
354 format in the dedicated particle database PARROT [27].

355 VTK files that represent cropped voxel-based regions of interest for ev-
356 ery particle from the tomographic reconstructions were used to recalculate
357 STL meshes for the particles, as some STL surfaces in the PARROT dataset
358 were not watertight, which would have led to problems in later analysis.
359 The STL data used in this study is available in the supplementary data.

360 Table 1 gives an overview of the six solids of which particle surface
361 data has been used. The particle size distributions are shown in the form
362 of cumulative sums in Fig. 7. Thee solids are typically in a particle size
363 range between 50 μm to 300 μm . The X-ray microscopy measurements were
364 performed for a final voxel size, i.e., edge length, of 2 μm .

365 2.2.2. Description

366 The properties of the six solids (cf. Table 1) are shown in Fig. 8. From
367 the plot of sphericity ψ_{Wa} over volume-equivalent diameter (Eqs.8 and 2)
368 in Fig. 8a, it can be seen that four solids—quartz, limestone, dolomite,
369 and aluminum oxide—are clustered in the same area with relatively high
370 sphericity values of $\psi_{Wa} > 0.5$. The soda-lime glass particles are the largest
371 and also have the highest sphericity values. The high sphericity values can

Table 1: Used particle systems, provided in the PARROT particle database [27]

type	production process	particle size	particles
aluminium oxide	crushing	55 μm to 200 μm	1571
dolomite	calcination and crushing	90 μm to 200 μm	642
soda-lime glass	spray drying	150 μm to 300 μm	602
limestone	dry milling	55 μm to 200 μm	1271
mica	comminution and magnetic separation	90 μm to 300 μm	415
quartz	crushing	< 200 μm	1656

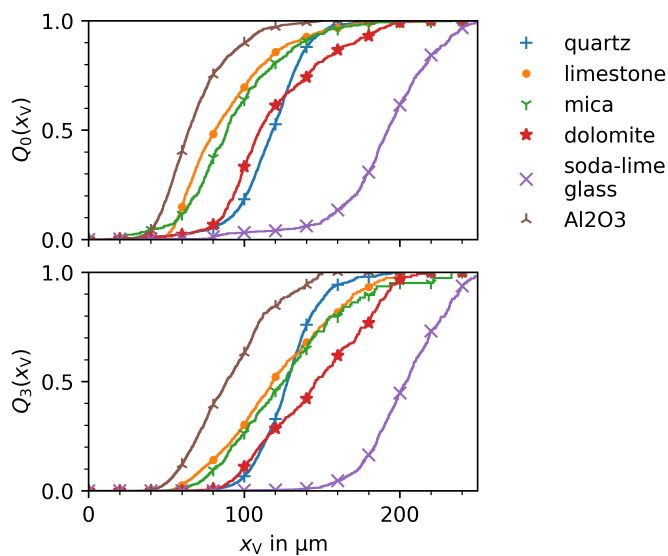


Figure 7: Number-base (Q_0) and volume-based (Q_3) particle size distributions for the six solids provided by the PARROT database

372 be traced to the production process by spray drying, resulting in mostly
 373 spherical shapes. In contrast, the mica particles show very low sphericities.

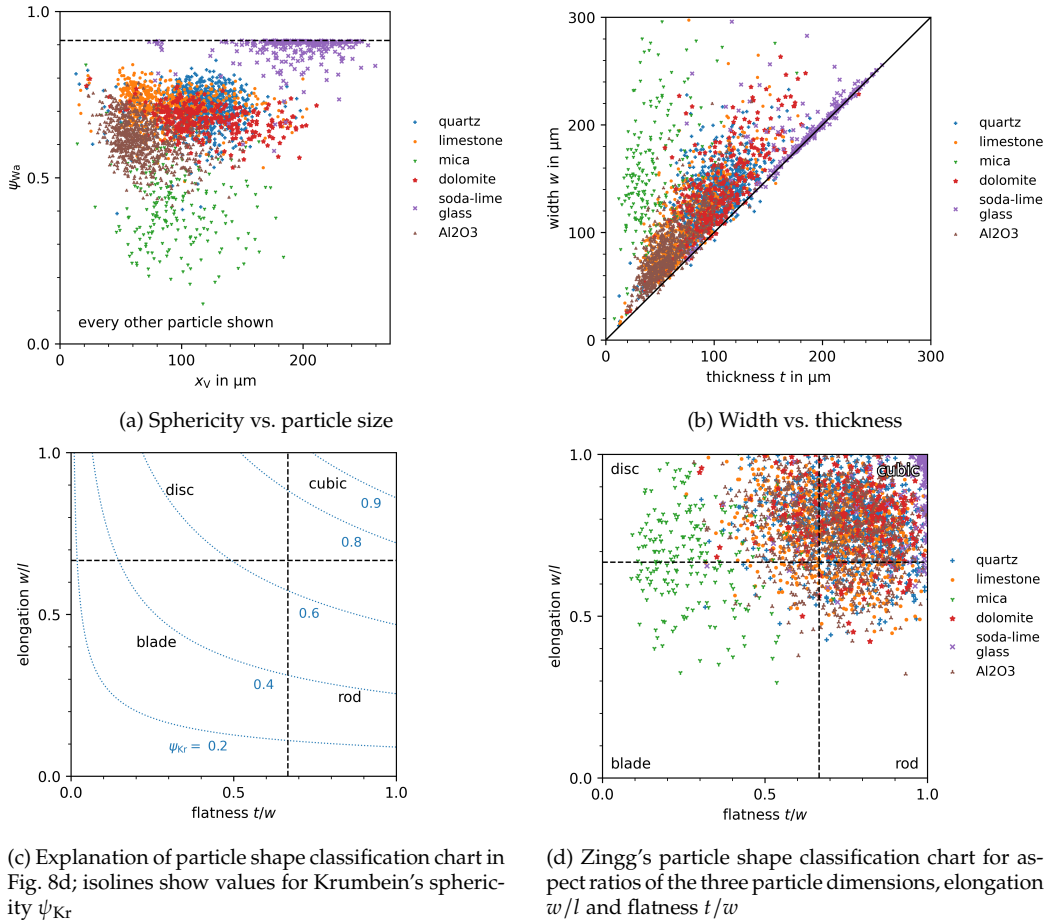


Figure 8: Properties of the six particle datasets

374 The maximum sphericity value of $\psi_{Wa} \approx 0.92$ stems from the conversion
 375 of the particle volumes from voxel representation to a triangular surface.
 376 The marching cubes algorithm interpolates between the edges of the vox-
 377 els to smooth the surface, depending on the number and configuration of
 378 adjacent solid voxels [47, 48]. The resulting error will be 8 % to 9 % [49].
 379 In comparison, the error in sphericity determination from the voxel repre-
 380 sentation for a sphere would be $> 30\%$, because of the greatly exaggerated
 381 surface area.

382 In Fig. 8d, the particles are plotted along two aspect ratios, flatness t/w
383 and elongation w/l , which makes classification according to particle shape
384 possible. l , w , and t are the three main dimensions of a particle: length,
385 width, and thickness, respectively, defined by the aligned bounding box
386 (cf. section 2.1.2). The plot was first introduced by Zingg and later devel-
387 oped by Krumbein and Janoo [11, 36, 50]. Fig. 8c serves as an explanation,
388 also showing isolines for sphericity, though Krumbein's sphericity defini-
389 tion is used, cf. Eq. 11. Alternative descriptors for the particle shape groups
390 "disc," "cubic," and "rod" are "oblate," "compact," and "prolate," respectively
391 [51].

392 Soda-lime glass spheres are expectedly clustered at values close to one
393 for both aspect ratios, while the majority of particles of the other solids
394 are mostly compact and could be classified as cubic and slightly rod- or
395 disc-shaped, depending on their particular flatness or elongation values.
396 In contrast, the mica particles are very flat and may be classified as disc-
397 and blade-like.

398 Fig. 9 provides an example for each of the four categories according to
399 the Zingg classification chart. The examples also serve to give an impres-
400 sion of what the different solids look like. While most of the limestone
401 and quartz particles can be classified as compact/cubic, the two particles
402 shown in Figs. 9a and 9d can be clearly identified as belonging to their re-
403 spective categories of disc- and rod-like. The soda-lime glass particles are
404 mostly near-perfect spheres, resulting in the aforementioned high spheric-
405 ity values. The mica is mostly flaky in nature, resulting in very low flatness
406 values, an effect that can be predicted from the plot of width vs. thickness
407 in Fig. 8b.

408 Because their properties are very similar, the group of quartz, limestone,
409 dolomite, and aluminum oxide will be grouped as "compact particles"
410 in section 3, while it will be instructive to see certain deviations for the
411 mica and soda-lime glass particles occur in the calculation of form factors
412 because of their unique shape properties.

413 2.3. 2D Imaging Simulation

414 2.3.1. Static Image Analysis

415 Static image analysis, as defined by ISO 13322-1, involves image acqui-
416 sition to determine particle size where the particles are not moving against
417 the axis of the optical equipment [52]. If a particle is large enough that
418 adhesion forces with respect to the surface it is resting on are negligible,

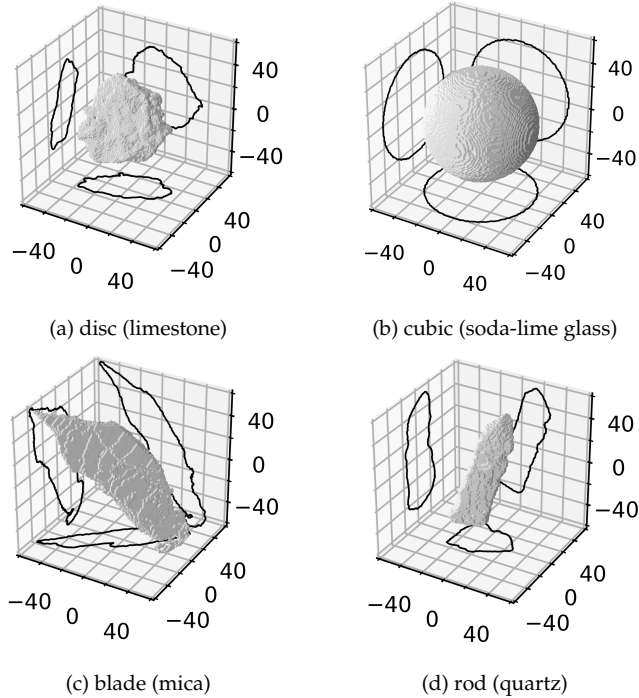


Figure 9: Examples from the datasets for particles belonging to the four shape categories of Figs. 8c and 8d with solid type in brackets

419 the particle will orient itself in a position in which at least its longest di-
 420 mension is measurable. Two possibilities for the simulation of static image
 421 analysis were calculated:

- 422 • alignment of the principal inertia vectors on the Cartesian axes and
- 423 • alignment of the particle in one of its stable resting positions.

424 3D manipulation of the provided STL files was done with the Python
 425 library `trimesh`, which, as the name implies, focuses on triangular meshes
 426 [53]. The `trimesh` package offers options for both the procedures named, in
 427 particular a method that returns a list of the most likely stable positions of
 428 a given mesh, containing both the necessary transform and the respective
 429 probability of the particle settling in this position. Any resting positions
 430 with a probability $p > 0.1$ were used for further 2D analysis. Because
 431 highly spherical particles can easily have no positions of especially high
 432 resting probability, for each particle *at least* the two most probable positions

433 were calculated. Fig. 10 gives an example of the stable positions of a particle
434 and the resulting projections, in this case in z -direction, i.e., onto the xy -
435 plane.

436 The imaging simulation involves getting the projection perpendicular
437 to the plane that acts as the resting surface when calculating the stable
438 position transforms (xy). For the mesh aligned along its principal inertia
439 vectors, the projection is calculated perpendicular to the plane that contains
440 the two major inertia vectors: when considering the aligned particle in
441 Fig. 4b, the projection would be in direction of the x vector, onto the yz
442 plane.

443 The subsequent procedure involves a custom function that calculates
444 the orthogonal projection of the triangular mesh onto a plane defined by
445 a given normal. With a given plane normal, the particle is first rotated to
446 the correct position, and a projection transform is performed onto the yz
447 (x -axis) plane (Fig. 1a). The projected triangles are then transformed into
448 a single 2D polygon using the Python package Shapely [54]. Thus, a single
449 contour is returned which can be used for further analysis. The relevant
450 code can be found in the supplementary materials, see section 5.

451 In principle, the effects of image resolution may be investigated by
452 scaling the projection and calculating a masked array that represents the
453 pixel image. However, pixelization in this sense has only been used for the
454 calculation of the enclosing and inscribed circles, cf. section 2.1.1.

455 2.3.2. *Dynamic Image Analysis*

456 In contrast to static analysis, dynamic image analysis is concerned with
457 the image acquisition and analysis of moving particles [55]. Particles are
458 therefore imaged in random orientations, unless the flow is highly turbu-
459 lent. Depending on the setup, particles may be imaged more than once if
460 they are not fast enough to leave the field of view. In many dynamic image
461 analysis devices, these images will be taken as separate particle entities,
462 while devices exist that track the particle while moving through the field
463 of view to measure as many rotations as possible, e.g., the Camsizer 3D
464 (Microtrac).

465 The procedure to produce a projection image is mostly the same as
466 before, except that the particle is first rotated randomly. For every parti-
467 cle, three random orientations were used to produce projections, thereby
468 increasing the number of simulated data points. Of course, the number
469 of projections can be increased at will; however, to stay in line with the

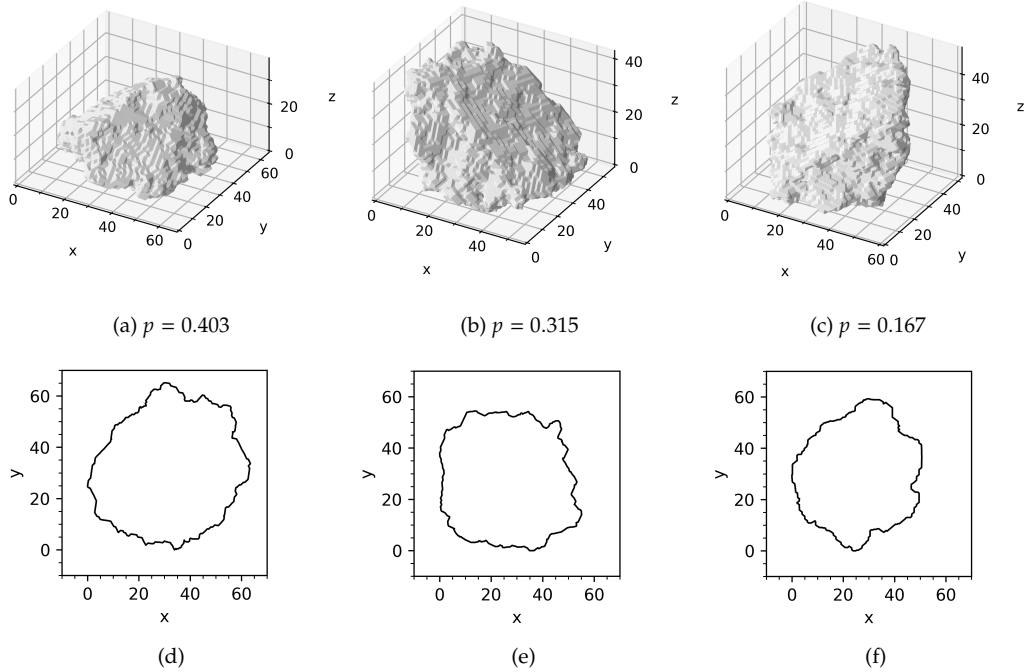


Figure 10: Stable position of the particle shown in Fig. 4 with the respective occurrence probabilities (Figs. 10a, 10b, and 10c) and resulting projection silhouettes along z -axis (Figs. 10d, 10e, and 10f)

470 number of projections achieved through the stable positions as described
 471 in the previous section, three positions were considered sufficient.

472 3. Simulation Results

473 With the methods given above, a dataset was produced that contains
 474 the properties of the 3D particles and properties of their respective projec-
 475 tions, produced in aligned, resting, and random orientations. The aligned
 476 orientations table naturally contains a single projection per particle, so
 477 6157 in total. The stable orientations table contains, on average, three pro-
 478 jections per particle for a total of 19 720 projections, though the absolute
 479 number per particle varies, cf. 3.2. For random orientations, every particle
 480 produced three projections, for a total of 18 471.

481 3.1. *Aligned Orientation*

482 The aligned projection dataset is in many ways the simplest one and is
483 used for verification of the analysis methods which are then used for the
484 datasets of stable orientations and random projections. Because there
485 is exactly one aligned projection for every particle, there are as many
486 projections as particles in the complete dataset of all solids, 6157 in total.
487 Because of the large number of particles, any effects found are considered
488 at least *interesting*, though maybe not statistically robust.

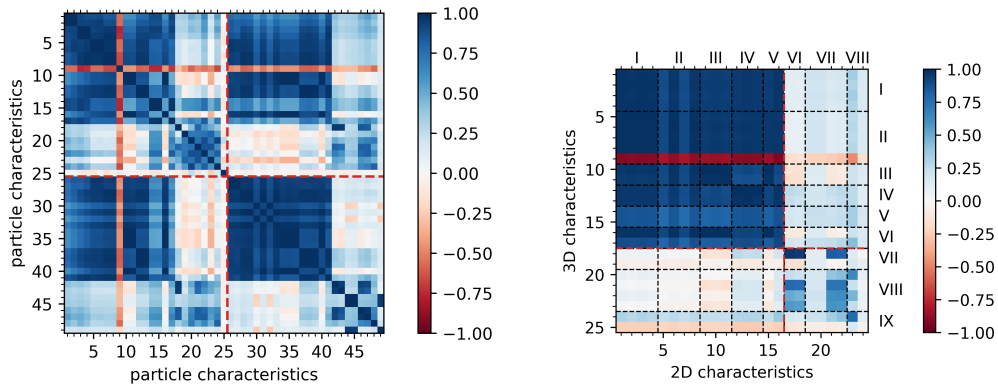
489 Overall, 49 particle characteristics are calculated and used to build a
490 correlation matrix, 25 comprising 3D and 24 comprising 2D measures and
491 descriptors. Table A.1 lists all particle characteristics. The characteristics
492 have been grouped into categories for easier comprehension of the corre-
493 lation matrix.

494 A resulting matrix of Pearson correlation coefficients is shown in Fig. 11a.
495 The resulting 49×49 grid contains many duplicates as well as areas not nec-
496 essarily interesting, like the correlation of 2D and 3D parameters against
497 themselves. The more interesting part of the matrix is the upper right or
498 lower left quadrant, where the correlations between 2D and 3D character-
499 istics are shown. This is why Fig. 11b only shows the upper right quadrant.
500 From Arabic numbers and Roman numerals a specific characteristic may
501 be determined with Table A.1.

502 Furthermore, only the compact particles (quartz, limestone, dolomite,
503 and aluminium oxide) are used to calculate the correlation matrices. This
504 is to avoid errors from the highly spherical soda-lime glass particles, as
505 discussed in section 2.2.2, and the much higher scatter introduced by the
506 plate-like mica.

507 Because some correlations are not linear, e.g., between equivalent diam-
508 eters and specific surface area, the Spearman rank coefficient is chosen over
509 the Pearson correlation coefficient. When comparing the two correlation
510 matrices of Fig. 11, the choice of the Spearman rank coefficient (Fig. 11b)
511 indeed results in much higher values. Values greater than zero will sig-
512 nify a positive correlation, whereas, if rarely, negative values will signify
513 negative correlations.

514 The comparison of different geometric measures and/or equivalent
515 diameters will result in very high correlations, as observed by the much
516 more pronounced coloring of the upper left area of Fig. 11b. The brighter
517 regions of less correlation are all in areas where shape factors are compared



(a) Correlation matrix showing standard correlation coefficient between all computed particle characteristics for all particles; 3D characteristics before, 2D after the dashed red line (b) Spearman rank correlation coefficient matrix for compact particles only

Figure 11: Correlation matrices for particle characteristics determined from *aligned projections*; Fig. 11b only shows the first quadrant (upper right) of the complete correlation matrix, with dashed red lines separating geometric properties and equivalent diameters from shape factors (cf. Table A.1)

518 with geometric measures, equivalent diameters, or other shape factors.
 519 This behavior should be expected, because geometric properties all scale
 520 with absolute particle size, while shape factors are limited to the unit
 521 interval $[0, 1]$.

522 The most fruitful task is to search for high coefficient values where
 523 2D and 3D shape factors are correlated, which is the lower right area of
 524 the correlation matrix in Fig. 11b. Because of the definition of particle
 525 dimensions via the bounding boxes, elongation w/l (18 in Fig. 11b) will
 526 correlate very well with aspect ratio AR (17), though the correlation with
 527 AR_{90} (18) naturally is perfect.

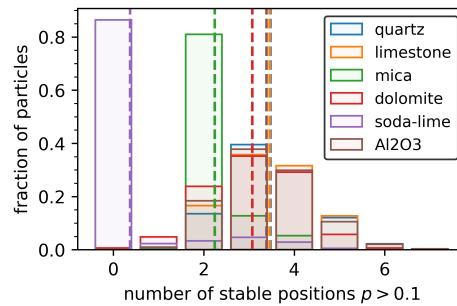
528 Interestingly, elongation (18) also correlates well with Wadell's alter-
 529 native circularity definition $\psi_{c,Wa}$ (21) and the bounding circles circularity
 530 ψ_{bc} (22). In a sense, ψ_{bc} forms a kind of aspect ratio, which is why it scales
 531 well with elongation: the inscribed d_{ic} and enclosed circle diameters d_{ec}
 532 show good correlation with minimum $x_{Fe,min}$ and maximum Feret diame-
 533 ters $x_{Fe,max}$, respectively. Krumbein sensibly took the square of elongation
 534 in his sphericity definition, Eq. 11, because elongation is a much better
 535 descriptor for the overall change from the cubic shape than flatness. In
 536 this sense, Krumbein's sphericity (21) shows pronounced, but not as high,
 537 correlations with the aspect ratios (17, 18) and Wadell's (21) and bounding

538 circles circularity (22). The relationship between $\psi_{c,Wa}$ and ψ_{bc} is briefly
 539 explored in appendix Appendix B.

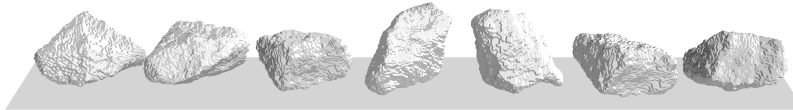
540 A final notable correlation is found between the 3D (24) and 2D solidities
 541 (23), indicating that 2D solidity is a good indicator of its 3D counterpart.
 542 However, the correlation is not linear and found to be $S_{x,3D} \approx S_{x,2D}^n$, with
 543 $n = 3$ to 4.

544 3.2. Stable Orientation

545 As described in section 2.3.1, at least the two most probable resting
 546 positions were used to produce projections. However, it is instructive to
 547 plot the distribution of stable positions with a probability $p > 0.1$ per solids
 548 type, as shown in Fig. 12a.



(a) Distribution of stable positions of all solids; dashed vertical lines indicate mean number of positions



(b) Stable positions of a single limestone particle

Figure 12: Stable positions of investigated solid particles for a position probability of $p > 0.1$

549 Again, the soda-lime glass and mica particles clearly deviate from the
 550 compact particles (quartz, limestone, dolomite, and aluminium oxide). The
 551 compact particles on average have three to four stable positions. There are
 552 some outliers at six and even seven stable positions. One limestone particle
 553 is shown in its seven stable positions in Fig. 12b. In contrast, the soda-lime
 554 glass spheres have no stable positions $p > 0.1$ for 80% of particles. The

555 flaky mica particles expectedly find stable resting positions only on either
 556 of their flat sides, and so obtain on average two stable positions.

557 For the simulation of static image analysis via stable positioning, the
 558 correlation matrix in Fig. 13a exhibits a slight drop in very high correla-
 559 tions. The correlations found between shape factors for aligned projections
 560 (Fig. 11b) are still present though.

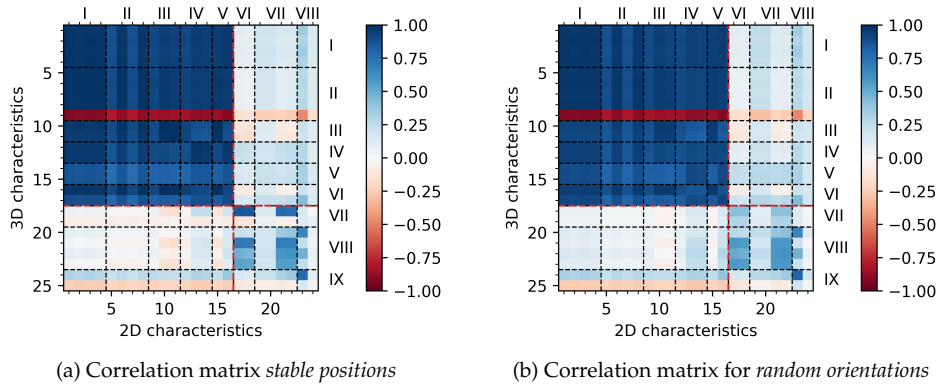


Figure 13: Correlation matrices of Spearman rank correlation coefficients for *compact particles* and *random orientations*; dashed red lines separate geometric properties and equivalent diameters from shape factors (cf. Table A.1)

561 A typical example of decreasing correlation coefficients are the 3D par-
 562 ticle widths (IV, 12/13) compared with minimum Ferets (12, 13) and 2D
 563 bounding box width (14). The reason is that a particle at an angle will
 564 not show its true width w anymore. Compared to the aligned projections,
 565 the correlation between elongation (18) and aspect ratios (VI, 17/18) is
 566 therefore slightly decreasing. Fig. 14 shows the correlation of several Feret
 567 diameters with their respective 3D particle dimensions. The perpendicular
 568 definition of minimum Feret $x_{\text{Fe},\text{min}90}$ scatters around the “true” particle
 569 width, whereas the true minimum Feret $x_{\text{Fe},\text{min}}$ systematically underesti-
 570 mates it. $x_{\text{Fe},\text{min}90}$ is therefore considered the more suitable estimate of
 571 particle width. Because of the definition of elongation w/l via the aligned
 572 bounding box, it will be better estimated by the orthogonal aspect ratio
 573 AR_{90} than the unaligned aspect ratio AR .

574 Of course, most correlations between 2D and 3D particle characteristics
 575 for static image analysis, as was discussed in this and the previous section,
 576 could have been found from careful thought experiments. Wadell based
 577 his alternative sphericity definition (Eq. 14) on a projection of a particle at

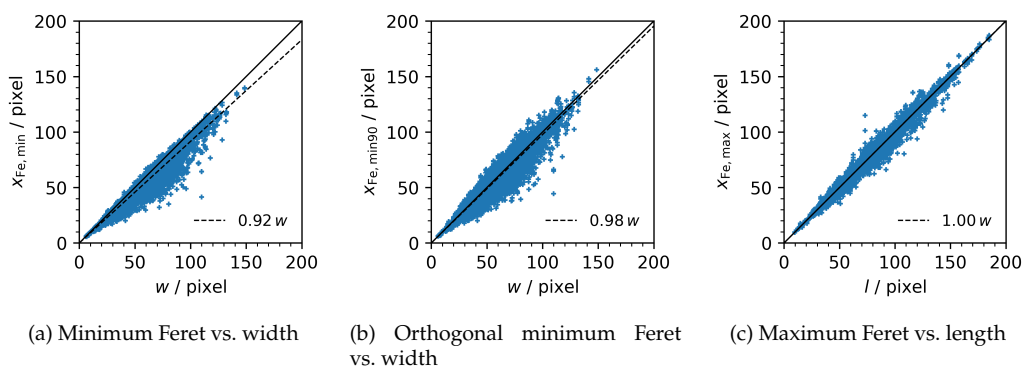


Figure 14: Comparison of Feret diameters to 3D measures for *all solids*

578 rest exactly because length and width should always be measurable in this
 579 situation, and most shape factors should scale with the derived aspect
 580 ratio/elongation, as long as the particles are not deviating too much from
 581 the cubic shape.

582 3.3. Random Orientation

583 When comparing the correlation matrices of the stable position analysis
 584 (Fig. 13a) and that for dynamic simulation, i.e., projections of particles
 585 at random orientations (Fig. 13b), the amount of correlation is notably
 586 decreasing.

587 Mostly, the properties of the 3D convex hull, V_c (2), $x_{V,c}$ (4), S_c (6),
 588 $x_{S,c}$ (8), and S_V (9) scale well with projection area-related characteristics
 589 A_c (1), x_A (2), A_c (3), and $x_{A,c}$ (4). Additionally, the 3D convex hull's
 590 surface area (6, 8) correlates well with the 2D convex hull's perimeter (6,
 591 8). However, remember that the Spearman rank correlation coefficient is
 592 used: correlations here need not be linear.

593 In case of the derived shape factors, the only good correlation exists be-
 594 tween 3D (24) and 2D solidity (23), $S_{x,3D}$ and $S_{x,2D}$, respectively. Otherwise,
 595 correlation between shape factors has decreased considerably.

596 In the following, relationships between 2D and 3D particle properties
 597 are investigated more closely. These investigations serve as examples on
 598 how the described dataset may be used for further insights by interested
 599 researchers.

600 **4. Correlations**

601 *4.1. Cauchy's Theorem*

602 The relationship between projection area and particle surface area is
 603 well known as Cauchy's theorem [56, 57]. Cauchy's theorem states that the
 604 surface area of a convex body $S_{p,c}$ is four times the projection area averaged
 605 over several projections $\overline{A_{p,c}}$.

$$S_{p,c} = 4\overline{A_{p,c}} \quad (20)$$

606 This theorem can be tested directly on the simulated data, not so much
 607 to prove the theorem, but to test the validity of the dataset. Fig. 15 shows the
 608 relations of surface area and projection area, both for the actual particles
 609 and their convex hulls. Note that single points are plotted, not actual
 610 averaged values, so Cauchy's theorem may only hold on the average, which
 611 is why linear regression lines are included. For the compact particle convex
 612 hulls (Fig. 15b), the value of 3.92 is particularly close to the theoretical
 613 value. For both soda-lime glass and mica the values decrease. For the
 614 mica particles, the lower regression value is expected, as it is very likely
 615 for a flaky particle to produce silhouettes of comparably lower projection
 616 area. For the soda-lime glass spheres, the lower result is due to the same
 617 inaccuracies of the mesh surface that lead to the maximum sphericity
 618 values of $\psi_{Wa} = 0.92$.

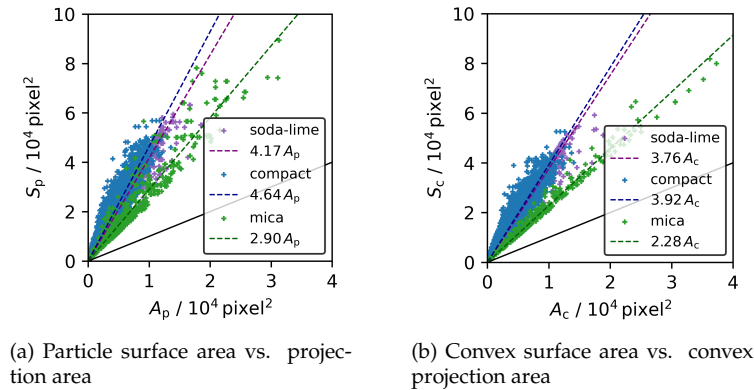


Figure 15: Correlations of surface area and projection area for *random orientations*

619 For the relation of actual particle surface and projection area, i.e., of the
 620 non-convex shapes, surface area is underestimated for both the compact

621 particles and the spherical soda-lime glass when compared to Cauchy's
 622 theorem. This trend is caused by the rugged surface, but may not be
 623 unique: for high surface roughnesses, projections may underestimate actual
 624 surface area [28]. In contrast, for mica particles, surface area is still
 625 grossly underestimated because the shape effect persists.

626 4.2. Sphericity-Circularity Correlation

627 Circularity ψ_c is often used in place of sphericity ψ_{Wa} because the former
 628 is much easier to measure in static or dynamic imaging setups [58]. It was
 629 therefore deemed a worthwhile exercise to see how well circularity and
 630 sphericity correlate for the dynamic imaging simulation.

631 Fig. 16 show plots of ψ_{Wa} and over ψ_c . The first insight is in regards to
 632 extremely small correlation values of the shape factors in the correlation
 633 matrices: at first sight, there is only a point cloud with no tendency what-
 634 soever. At second sight, because of the nature of the two shape factors, both
 635 should be zero for infinitely stretched objects and one for spheres. Because
 636 of this unique relationship, a linear regression needs no offset, i.e., should
 637 start from zero. If a linear regression then returns a slope of one, the two
 638 shape factors are perfectly correlated. Any spread in either direction is
 639 then purely stochastic. The term "stochastic" here signifies the inherent
 640 scatter of imaging particles at random orientations, not measurement error.

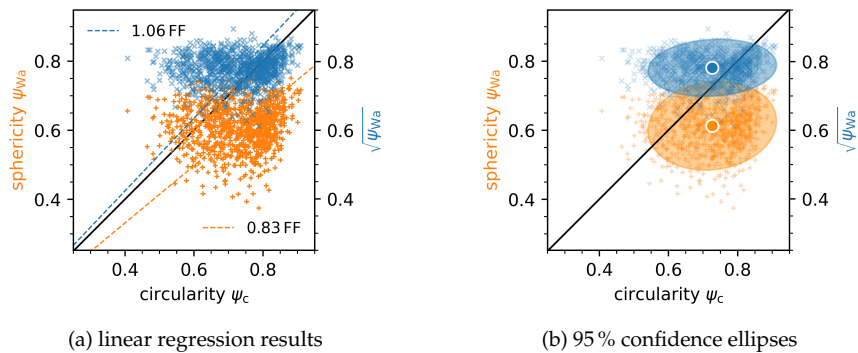


Figure 16: Correlation of sphericity and its square root with form factor for alumina particles (Al_2O_3) at random orientations

641 From Fig. 16a it can be seen that the correlation between circularity ψ_c
 642 and sphericity ψ_{Wa} is rather non-ideal, whereas the square root of sphericity
 643 $\sqrt{\psi_{Wa}}$ leads a much better linear regression slope of 1.06. Another way

644 to evaluate the two parameter pairs is to plot the 95 % confidence interval
645 (CI). Because the data is two-dimensional, confidence ellipses are calcu-
646 lated, as shown in Fig. 16b. As shown, the center of the ellipse of $\sqrt{\psi_{Wa}}$
647 vs. ψ_c (in blue) is much closer to the equality line then the ellipse for ψ_{Wa}
648 vs. ψ_c (in orange).

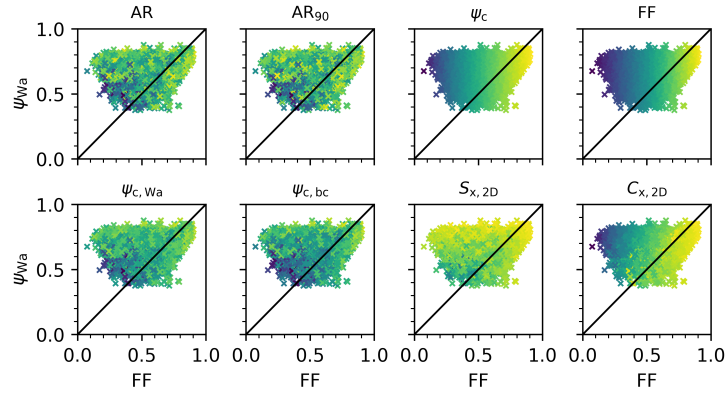
649 Squaring the new-found relationship gives sphericity ψ_{Wa} over the form
650 factor $FF = \psi_c^2$. However, the correlation of sphericity and form factor is
651 far from providing a reliable predictor for sphericity from 2D particle
652 projection measurements.

653 To find if there is an underlying variable with which the data could be
654 corrected, the data for all compact solids (quartz, limestone, dolomite, and
655 aluminium oxide) was plotted as shown in Fig. 17a. We will call Fig. 17a
656 the parameter plot, as it shows how parameters scale within a correlation.
657 The plots all show the same relationship, but individual points are plotted
658 with a color map that scales according to a third parameter. To make
659 any relationship, if existing, clear, the color map always scales between
660 the smallest and the largest value of the chosen parameter. In the case of
661 circularity and form factor, we can see a smooth color band from left to
662 right, which makes sense, given that the plot's x -axis is the form factor.
663 To correct the point cloud to scatter more evenly around the equality line,
664 there needs to be a parameter that changes monotonously from the upper
665 left to the lower right of the graph, i.e., orthogonally to the equality line.
666 Solidity, for example, is a poor candidate because it decreases in direction
667 of the y -axis.

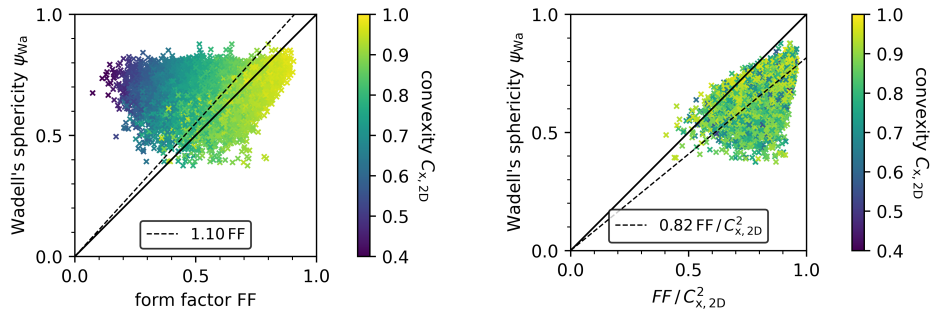
668 In contrast, 2D convexity $C_{x,2D}$ fulfills the described relationship for the
669 given data, with the smallest values found in the upper left corner, and
670 values decreasing toward the equality line. Fig. 17b displays the same plot
671 with a color bar for the convexity values. The parameter is thus a good
672 candidate to correct the linear relationship of form factor and sphericity: if
673 the form factor is divided by the 2D convexity, points in the upper left of
674 the plot will move to the right, while points close to the equality line will
675 stay there, as their convexity values are already close to one.

676 In fact, if the form factor is divided by the square of 2D convexity $C_{x,2D}^2$,
677 there is, at least visually, no correlation of the data with the parameter at
678 all anymore, as shown in Fig. 17c. However, the correlation to sphericity
679 has worsened, with a regression slope of only 0.82.

680 The procedure is thus repeated with a new parameter plot that contains

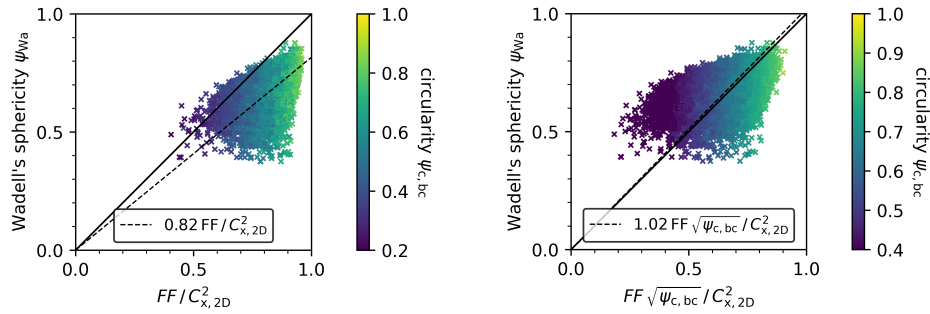


(a) Parameter plot for Wadell's sphericity vs. form factor



(b) Influence of 2D convexity

(c) Correlation with 2D convexity



(d) Influence of bounding circles circularity

(e) Correlation with bounding circles circularity

Figure 17: Pathway to a correlation of 2D shape factors and Wadell's sphericity; only compact particles (no soda-lime glass and mica) at random rotations are shown; final result in Fig. 18

681 the x - and y -axes of the new correlation. The next candidate shape factor,
 682 that fulfills the requirements described above is the bounding circles circu-
 683 larity $\psi_{c,bc}$, as shown in Fig. 17d. The shape factor can be used to produce
 684 an excellent correlation by “stretching” the data back to the equality line,
 685 Fig. 17e. The regression slope is now almost perfect at 1.02. Furthermore,
 686 the resulting correlation exhibits expected behavior for a correlation of cir-
 687 cularity and sphericity: at high values approaching one, there is little error
 688 in the prediction, while the error widens as the values decrease, because
 689 there is a higher fluctuation in the projection images that can be produced
 690 for more irregular particles.

691 The correlation thus found is:

$$\psi_{Wa} \approx FF \sqrt{\psi_{c,bc}} / C_{x,2D}^2 \quad (21)$$

692 Several other equations were tested concerning their relevance for the
 693 given solids, i.e., for their predictive power with regards to Wadell’s
 694 sphericity. The simplest correlation is the one found for before:

$$\psi_{Wa} \approx FF \quad (22)$$

695 For the two equations average sphericity predictions were calculated.
 696 The results are summarized in Table 2. Eq. 21 is clearly superior compared
 697 to Eq. 22. Only in the case of mica, Eq. 22 provides a better average
 698 estimate of sphericity, which may hint at the simpler correlation being
 699 more accurate in the case of plate-like particles. There is even an argument
 700 that the standard deviation of predicted sphericity values is about twice as
 701 large as the true scatter of sphericities, so that even the standard deviation
 702 $\sigma(\psi_{Wa})$ of the 3D particles can be estimated.

703 Fig. 18 shows the resulting correlation of Eq. 21 for all solids. As pre-
 704 viously determined, there is significant error for soda-lime glass particles
 705 at very high sphericities due to the nature of the meshed surfaces, which
 706 results in the lowest slope of the cubic/compact particles. For mica, the
 707 correlation is especially poor, though the average predicted sphericity is
 708 only about 5 % off from the actual value.

709 Note that the predictive value is reasonably good because of the large
 710 number of data points. If there had been only a handful of particles, the
 711 final correlation would have been nearly impossible to find. Furthermore,
 712 the predictive power may not hold for all types of solids, especially because
 713 of the use of convexity. If surface roughness significantly increases, surface

Table 2: Average sphericities determined with the correlation equations 21 through 22; intervals shown are the standard deviations form the mean, coefficients of determination r^2 are for linear fits as in Fig. 18

material		equation		
		3D	21	22
quartz	ψ_{Wa}	0.71 ± 0.05	0.69 ± 0.09	0.63 ± 0.16
	r^2	–	0.985	0.943
limestone	ψ_{Wa}	0.72 ± 0.05	0.65 ± 0.11	0.58 ± 0.16
	r^2	–	0.982	0.928
mica	ψ_{Wa}	0.42 ± 0.11	0.44 ± 0.17	0.43 ± 0.13
	r^2	–	0.824	0.911
dolomite	ψ_{Wa}	0.68 ± 0.04	0.68 ± 0.09	0.58 ± 0.12
	r^2	–	0.986	0.958
soda-lime	ψ_{Wa}	0.89 ± 0.05	0.93 ± 0.11	0.76 ± 0.18
	r^2	–	0.995	0.945
Al ₂ O ₃	ψ_{Wa}	0.61 ± 0.06	0.61 ± 0.10	0.54 ± 0.13
	r^2	–	0.976	0.939

714 area effects could be underestimated by 2D convexity [28]. Because the
715 resolution of STL mesh, voxel image, and projection silhouette are directly
716 linked and should be identical, the correlation is expected to give sphericity
717 values *at the same resolution* for the surface area of the particle.

718 How could Eq. 21 be used in practice? It needs to be understood that
719 this correlation is not able to predict sphericities of single particles, which
720 is apparent form the scatter in Fig. 18a. However, what the correlation
721 can achieve is the prediction of a mean sphericity for a given bulk solids,
722 which is in most cases the only needed information. This is highlighted
723 in a plot of the relative error of the correlation, Fig. 18c. Where there are
724 enough particles, the mean predicted sphericity is well within 5% of the
725 true value. In contrast, the 95 % CI scatters about $\pm 35\%$ around the actual
726 value, so single-shot estimates are highly unreliable.

727 4.3. Particle Width–Feret Correlation

728 As mentioned in the introduction, dynamic image analysis is widely
729 used to replace sieve analysis. More often than not, data from a dynamic
730 image analysis system needs to be adjusted to account for divergence of
731 the measurements from a sieve analysis. When sieving is done on square

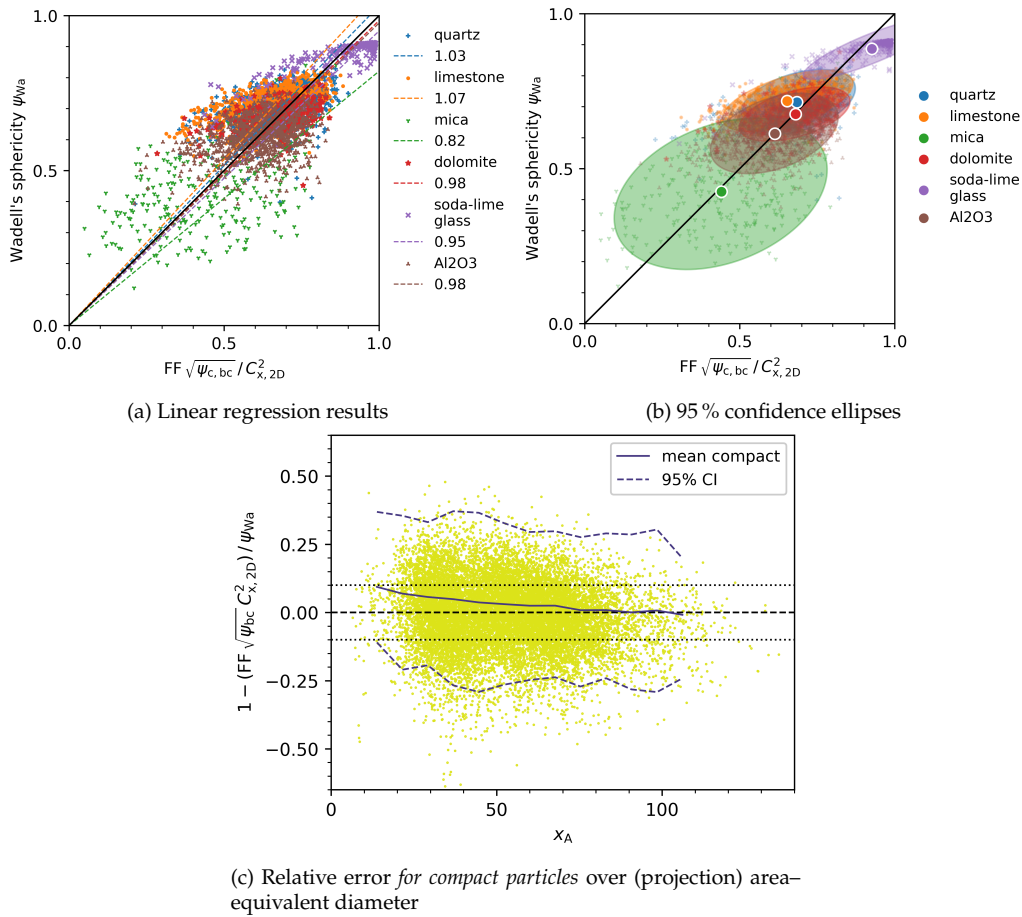


Figure 18: Correlation of 2D shape factors and Wadell's sphericity for the dynamic image analysis case (*random orientations*)

732 aperture sieve meshes, particles will be classified according to their
 733 intermediate dimension, width w . In static image analysis, particle width is
 734 very well determined by the minimum Ferets, $x_{\text{Fe,min}}$ or $x_{\text{Fe,min}90}$ (cf. Fig 14).
 735 However, in dynamic image analysis it is only possible to know the three
 736 main particle dimensions l , w , and t through imaging of particle from dif-
 737 ferent angles or by tracking rotating particles while they fall through the
 738 measurement system [26, 59].

739 Using the methods detailed in the previous section, aspect ratio AR
 740 was found to be the underlying variable explaining the deviation of both
 741 the minimum $x_{\text{Fe,min}}$ and maximum Feret diameters $x_{\text{Fe,max}}$ from particle

742 width w . The following correlation was found to predict particle width
 743 very well:

$$w \approx x_{\text{Fe,max}} \sqrt{\text{AR}} \quad (23)$$

744 Furthermore, because of the definition of aspect ratio, Eq. 6:

$$w \approx x_{\text{Fe,max}} \sqrt{\text{AR}} = \frac{x_{\text{Fe,min}}}{\sqrt{\text{AR}}} = \sqrt{x_{\text{Fe,max}} x_{\text{Fe,min}}} \quad (24)$$

745 The correlation defined by Eq. 23 is shown in Fig. 19a. For the compact
 746 particles, the agreement between 2D and 3D parameters is quite excellent.
 747 Even for the non-compact mica particles, the correlation holds, though
 748 the scatter is expectedly larger. Fig. 19b gives the relative deviation of
 749 width estimates from actual particle width. For compact particles, the
 750 95 % confidence interval is within a deviation of $\pm 25\%$, while the mean is
 751 within a $\pm 5\%$ interval.

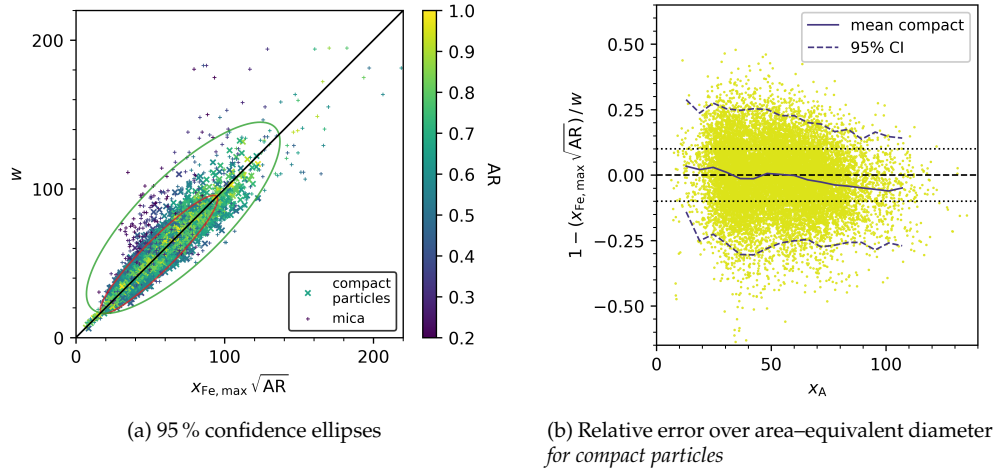


Figure 19: Correlation of Feret diameters with particle width w

752 The relevant particle dimension for sieve analysis, width w , is therefore
 753 expected to be approximated well with any of the expressions of Eq. 24.

754 5. Conclusions

755 A collection of particle surface meshes, resulting from X-ray tomo-
 756 graphic measurements, has been used to simulate both static and dynamic

757 image analysis. The results have been evaluated to find the highest cor-
758 relations between 2D and 3D geometric measures and shape factors. The
759 dataset and methods described prove to be physically accurate, although
760 highly spherical soda-lime glass particles reach a final sphericity lower
761 than one because of the nature of the description of particle surfaces as
762 triangular meshes.

763 Examples have been given of the potential insights this dataset may
764 generate. A correlation between Wadell's sphericity in 3D and the form
765 factor in 2D has been found that is expected to predict sphericity values well
766 for a wide range of particles, provided that enough particles are measured.
767 In the same vein, a correlation for estimating particle width from 2D Feret
768 diameters has been determined. Confirmation experiments with a broader
769 set of particles are planned in the future. An inherent measurement artifact
770 of image analysis, pixel resolution, needs to be investigated before the
771 correlations found are implemented in measurement setups.

772 The dataset, as provided in the supplementary data, offers the possi-
773 bility to discover numerous correlations and insights regarding geometric
774 measures and shape factors, as well as their relationships across two and
775 three dimensions. We encourage researchers to use the dataset for their
776 research questions and to shed light into questions that had long been
777 obscured by computational complexity.

778 **Supplementary Data**

779 Supplementary files are available in the Open Access Repository and
780 Archive for Research Data of Saxon Universities (OPARA):

781 <https://doi.org/10.25532/OPARA-479>

782 Supplementary files enable users to reproduce imaging datasets as used
783 in this study and demonstrate the methods for acquisition of all particle
784 characteristics for an example particle. Particle STL files and the resulting
785 dataset tables are included. Note that you need a working Python setup
786 and that all code is made available as Jupyter notebooks.

787 **Acknowledgements**

788 This research work was supported by the German Federal Ministry of
789 Education and Research through the research project InfraDatRec (grant
790 no. 03XP0426A).

791 **Appendix A. Particle characteristics**

792 Table A.1 gives a list of the particle characteristics as used in the corre-
 793 lation matrices, Figs. 11 and 13.

794 **Appendix B. Wadell's Circularity**

795 One correlation found, that is not necessarily expected, is between
 796 Wadell's alternative circularity definition $\psi_{c,Wa}$ (Eq. 14) and the bounding
 797 circles circularity $\psi_{c,bc}$ (Eq. 15). Though it is a correlation between two 2D
 798 shape factors, it is too interesting to ignore. As predicted by the correlation
 799 matrix in Fig. 11a, where the correlation is found in the lower right (second)
 800 quadrant between values 46 ($\psi_{c,Wa}$) and 47 ($\psi_{c,bc}$), there is a near perfect
 801 linear relationship. However, to have the two circularities directly coincide,
 802 Wadell's circularity is squared, $\psi_{c,Wa}^2$. The resulting correlation is shown
 803 in Fig. B.1a.

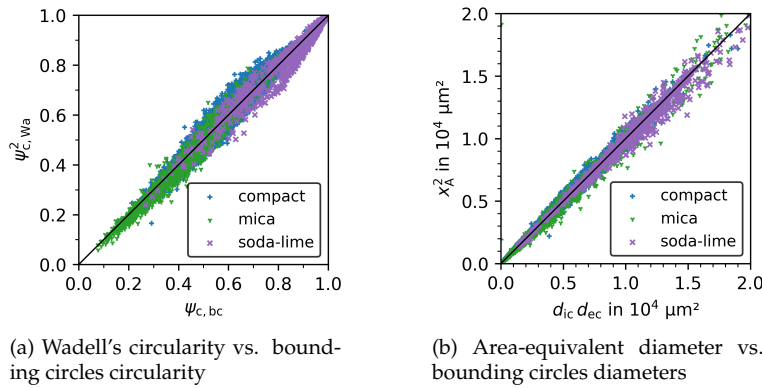


Figure B.1: Correlation of Wadell's alternative definition for circularity (Eq. 14) and bounding circles circularity (Eq. 15)

804 Because of the definitions of the two circularities, it is found that the
 805 area-equivalent diameter is directly related to the bounding circle diame-
 806 ters.

$$x_A^2 \approx d_{ic} d_{ec} \quad (B.1)$$

807 The above relationship is shown in Fig. B.1b.

Table A.1: Particle characteristics

no.	category	name	symbol	dimensions	equation	
3D characteristics						
1	I	particle volume	V_p	L^3	–	
2		convex volume	V_c	L^3	–	
3		volume-equivalent diameter	x_V	L^1	2	
4		convex volume-eq. diameter	$x_{V,c}$	L^1	–	
5	II	particle surface area	S_p	L^2	–	
6		convex surface area	S_c	L^2	–	
7		surface-equivalent diameter	x_S	L^1	3	
8		convex surface-eq. diameter	$x_{S,c}$	L^1	–	
9		volume-specific surface area	S_V	L^{-1}	–	
10	III	aligned length	l	L^1	–	
11		oriented length	l_{oriented}	L^1	–	
12	IV	aligned width	w	L^1	–	
13		oriented width	w_{oriented}	L^1	–	
14	V	aligned thickness	t	L^1	–	
15		oriented thickness	t_{oriented}	L^1	–	
16	VI	min. enclosing sphere diameter	d_{es}	L^1	–	
17		max. inscribed sphere diameter	d_{is}	L^1	–	
18	VII	elongation	w/l	–	–	
19		flatness	t/w	–	–	
20	VIII	Wadell's sphericity	ψ_{Wa}	–	8	
21		Krumbein's sphericity	ψ_{Kr}	–	11	
22		bounding spheres sphericity	ψ_{Wa}	–	9	
23		Hofmann's sphericity	ψ_{Ho}	–	10	
24	IX	3D solidity	$S_{x,3D}$	–	16	
25		3D convexity	$C_{x,3D}$	–	18	
2D characteristics						
26	1	I	projection area	A_p	L^2	–
27	2		convex projection area	A_c	L^2	–
28	3		area-equivalent diameter	x_A	L^1	4
29	4		convex area-eq. diameter	$x_{A,c}$	L^1	–
30	5	II	projection perimeter	P_p	L^1	–
31	6		convex projection perimeter	P_c	L^1	–
32	7		perimeter-equivalent diameter	x_P	L^1	5
33	8		convex perimeter-eq. diameter	$x_{P,c}$	L^1	–
34	9	III	bounding box length	l_{bb}	L^1	–
35	10		maximum Feret diameter	$x_{Fe,max}$	L^1	–
36	11		orthogonal Feret to $x_{Fe,min}$	$x_{Fe,max90}$	L^1	–
37	12	IV	bounding box width	w_{bb}	L^1	–
38	13		minimum Feret diameter	$x_{Fe,min}$	L^1	–
39	14		orthogonal Feret to $x_{Fe,max}$	$x_{Fe,min90}$	L^1	–
40	15	V	min. enclosing circle diameter	d_{ec}	L^1	–
41	16		max. inscribed circle diameter	d_{ic}	L^1	–
42	17	VI	aspect ratio	AR	–	–
43	18		orthogonal aspect ratio	AR ₉₀	–	–
44	19	VII	circularity	ψ_c	–	12
45	20		form factor	FF	–	13
46	21		Wadell's circularity	$\psi_{c,Wa}$	–	14
47	22		bounding circles circularity	$\psi_{c,bc}$	–	15
48	23	VIII	2D solidity	$S_{x,2D}$	–	17
49	24		2D convexity	$C_{x,2D}$	–	19

808 **References**

- 809 [1] T. Buchwald, E. Schach, U. A. Peuker, A framework for the description
810 of multidimensional particle separation processes, *Powder Technol-*
811 *ogy* 433 (2024) 119165. doi:10.1016/j.powtec.2023.119165.
- 812 [2] E. Schach, T. Buchwald, T. Leißner, U. Peuker, R. T. Delgado, Concepts
813 of entropy for raw materials, *Powder Technology* 435 (2024) 119398.
814 doi:10.1016/j.powtec.2024.119398.
- 815 [3] U. Ulusoy, C. Igathinathane, Particle size distribution modeling of
816 milled coals by dynamic image analysis and mechanical sieving, *Fuel*
817 *Processing Technology* 143 (2016) 100–109. doi:10.1016/j.fuproc.
818 2015.11.007.
- 819 [4] J. Fernlund, 3-d image analysis size and shape method applied to
820 the evaluation of the los angeles test, *Engineering Geology* 77 (2005)
821 57–67. doi:10.1016/j.enggeo.2004.08.002.
- 822 [5] S. Durand, B. E. Jackson, W. C. Fonteno, J. Michel, Particle size distri-
823 bution of growing media constituents using dynamic image analysis:
824 Parametrization and comparison to sieving, *Soil Science Society of*
825 *America Journal* 87 (2023) 767–780. doi:10.1002/saj2.20518.
- 826 [6] J. Emmerich, Q. Tang, Y. Wang, P. Neubauer, S. Junne, S. Maaß, Optical
827 inline analysis and monitoring of particle size and shape distributions
828 for multiple applications: Scientific and industrial relevance, *Chinese*
829 *Journal of Chemical Engineering* 27 (2019) 257–277. doi:10.1016/j.
830 cjche.2018.11.011.
- 831 [7] D. M. Scott, Recent advances in in-process characterization of
832 suspensions and slurries, *Powder Technology* 399 (2022) 117159.
833 doi:10.1016/j.powtec.2022.117159.
- 834 [8] H. Wadell, Volume, shape, and roundness of rock particles., *The*
835 *Journal of Geology* 40 (1932) 443–451.
- 836 [9] H. Wadell, Sphericity and roundness of rock particles, *The Journal of*
837 *Geology* 41 (1933) 310–331. doi:10.1086/624040.

- 838 [10] B. C. Aschenbrenner, A new method of expressing particle sphericity, *SEPM Journal of Sedimentary Research* 26 (1956). doi:10.1306/74d704a7-2b21-11d7-8648000102c1865d.
- 839
840
- 841 [11] Zingg, Theodor, *Beitrag zur Schotteranalyse*, Ph.D. thesis, ETH Zürich, 1935. doi:10.3929/ETHZ-A-000103455.
- 842
- 843 [12] V. Angelidakis, S. Nadimi, S. Utili, Shape analyser for particle engineering (shape): Seamless characterisation and simplification of particle morphology from imaging data, *Computer Physics Communications* 265 (2021) 107983. doi:10.1016/j.cpc.2021.107983.
- 844
845
846
- 847 [13] T. Yao, W. Li, Quantifying the particle shape and surface roughness of sands, *Bulletin of Engineering Geology and the Environment* 82 (2023). doi:10.1007/s10064-023-03167-7.
- 848
849
- 850 [14] D. Su, W. M. Yan, Prediction of 3d size and shape descriptors of irregular granular particles from projected 2d images, *Acta Geotechnica* 15 (2019) 1533–1555. doi:10.1007/s11440-019-00845-3.
- 851
852
- 853 [15] X. Wang, K. Tian, D. Su, J. Zhao, Superellipsoid-based study on reproducing 3d particle geometry from 2d projections, *Computers and Geotechnics* 114 (2019) 103131. doi:10.1016/j.compgeo.2019.103131.
- 854
855
856
- 857 [16] W.-Q. Xie, X.-P. Zhang, X.-M. Yang, Q.-S. Liu, S.-H. Tang, X.-B. Tu, 3d size and shape characterization of natural sand particles using 2d image analysis, *Engineering Geology* 279 (2020) 105915. doi:10.1016/j.enggeo.2020.105915.
- 858
859
860
- 861 [17] C. H. Lee, S. J. Lee, M. Shin, Characterization of variability in 2-dimensional particle geometry via 3d structured light scanning, *Transportation Geotechnics* 34 (2022) 100760. doi:10.1016/j.trgeo.2022.100760.
- 862
863
864
- 865 [18] X. Jia, R. Liu, H. Ren, Y. Han, J. Ouyang, H. Zheng, C. Peng, J. Zheng, Particle shape characterizations for energetic materials by computational geometry and stereology method, *SN Applied Sciences* 4 (2022). doi:10.1007/s42452-022-05031-x.
- 866
867
868

- 869 [19] R. D. Beemer, L. Li, A. Leonti, J. Shaw, J. Fonseca, I. Valova, M. Iskan-
870 der, C. H. Pilskaln, Comparison of 2d optical imaging and 3d micro-
871 tomography shape measurements of a coastal bioclastic calcareous
872 sand, *Journal of Imaging* 8 (2022) 72. doi:10.3390/jimaging8030072.
- 873 [20] G. Bagheri, C. Bonadonna, I. Manzella, P. Vonlanthen, On the charac-
874 terization of size and shape of irregular particles, *Powder Technology*
875 270 (2015) 141–153. doi:10.1016/j.powtec.2014.10.015.
- 876 [21] G. Mollon, J. Zhao, 3d generation of realistic granular samples based
877 on random fields theory and fourier shape descriptors, *Computer*
878 *Methods in Applied Mechanics and Engineering* 279 (2014) 46–65.
879 doi:10.1016/j.cma.2014.06.022.
- 880 [22] T. Ueda, Estimation of three-dimensional particle size and shape
881 characteristics using a modified 2d–3d conversion method employ-
882 ing spherical harmonic-based principal component analysis, *Powder*
883 *Technology* 404 (2022) 117461. doi:10.1016/j.powtec.2022.117461.
- 884 [23] P. Zhang, Z. Yin, Y. Jin, Three-dimensional quantitative analysis on
885 granular particle shape using convolutional neural network, *Interna-*
886 *tional Journal for Numerical and Analytical Methods in Geomechan-*
887 *ics* 46 (2021) 187–204. doi:10.1002/nag.3296.
- 888 [24] K. Giannis, C. Thon, G. Yang, A. Kwade, C. Schilde, Predicting 3d
889 particles shapes based on 2d images by using convolutional neural net-
890 work, *Powder Technology* 432 (2024) 119122. doi:10.1016/j.powtec.
891 2023.119122.
- 892 [25] C. Rao, E. Tutumluer, J. Stefanski, Coarse aggregate shape and size
893 properties using a new image analyzer, *Journal of Testing and Evalu-*
894 *ation* 29 (2001) 461–471. doi:10.1520/jte12276j.
- 895 [26] A. K. Rajagopalan, J. Schneeberger, F. Salvatori, S. Bötschi, D. R.
896 Ochsenbein, M. R. Oswald, M. Pollefeys, M. Mazzotti, A comprehen-
897 sive shape analysis pipeline for stereoscopic measurements of par-
898 ticulate populations in suspension, *Powder Technology* 321 (2017)
899 479–493. doi:10.1016/j.powtec.2017.08.044.
- 900 [27] R. Ditscherlein, O. Furat, E. Löwer, R. Mehnert, R. Trunk, T. Leißner,
901 M. J. Krause, V. Schmidt, U. A. Peuker, Parrot: A pilot study on

- 902 the open access provision of particle-discrete tomographic datasets,
903 Microscopy and Microanalysis 28 (2022) 350–360. doi:10.1017/
904 s143192762101391x.
- 905 [28] T. Buchwald, G. Schmandra, L. Schützenmeister, T. Fraszczak,
906 T. Mütze, U. Peuker, Gaseous flow through coarse granular beds:
907 The role of specific surface area, Powder Technology 366 (2020) 821–
908 831. doi:10.1016/j.powtec.2020.03.028.
- 909 [29] G. Bradski, The OpenCV Library, Dr. Dobb’s Journal of Software
910 Tools (2000).
- 911 [30] P. Virtanen, R. Gommers, T. E. Oliphant, M. Haberland, T. Reddy,
912 D. Cournapeau, E. Burovski, P. Peterson, W. Weckesser, J. Bright, S. J.
913 van der Walt, M. Brett, J. Wilson, K. J. Millman, N. Mayorov, A. R. J.
914 Nelson, E. Jones, R. Kern, E. Larson, C. J. Carey, Í. Polat, Y. Feng, E. W.
915 Moore, J. VanderPlas, D. Laxalde, J. Perktold, R. Cimrman, I. Hen-
916 riksen, E. A. Quintero, C. R. Harris, A. M. Archibald, A. H. Ribeiro,
917 F. Pedregosa, P. van Mulbregt, SciPy 1.0 Contributors, SciPy 1.0: Fun-
918 damental Algorithms for Scientific Computing in Python, Nature
919 Methods 17 (2020) 261–272. doi:10.1038/s41592-019-0686-2.
- 920 [31] B. Zhao, J. Wang, 3d quantitative shape analysis on form, roundness,
921 and compactness with μct , Powder Technology 291 (2016) 262–275.
922 doi:10.1016/j.powtec.2015.12.029.
- 923 [32] J. Zheng, R. D. Hryciw, Traditional soil particle sphericity, roundness
924 and surface roughness by computational geometry, Géotechnique 65
925 (2015) 494–506. doi:10.1680/geot.14.p.192.
- 926 [33] D. Legland, I. Arganda-Carreras, P. Andrey, Morpholibj: integrated
927 library and plugins for mathematical morphology with imagej, Bioin-
928 formatics 32 (2016) 3532–3534. doi:10.1093/bioinformatics/btw413.
- 929 [34] G. Lehmann, D. Legland, Efficient n-dimensional surface estimation
930 using crofton formula and run-length encoding, The Insight Journal
931 (2012). doi:10.54294/wdu86d.
- 932 [35] C. Lang, J. Ohser, R. Hilfer, On the analysis of spatial binary im-
933 ages, Journal of Microscopy 203 (2001) 303–313. doi:10.1046/j.
934 1365-2818.2001.00899.x.

- 935 [36] W. C. Krumbein, Measurement and geological significance
936 of shape and roundness of sedimentary particles, SEPM
937 Journal of Sedimentary Research Vol. 11 (1941). doi:10.1306/
938 d42690f3-2b26-11d7-8648000102c1865d.
- 939 [37] J. W. Bullard, E. J. Garboczi, Defining shape measures for 3d star-
940 shaped particles: Sphericity, roundness, and dimensions, Powder
941 Technology 249 (2013) 241–252. doi:10.1016/j.powtec.2013.08.015.
- 942 [38] H. J. Hofmann, Grain-shaped indices and isometric graphs,
943 Journal of Sedimentary Research 64 (1994) 916–920. doi:10.1306/
944 d4267f0a-2b26-11d7-8648000102c1865d.
- 945 [39] J. P. Le Roux, Comparison of sphericity indices as re-
946 lated to the hydraulic equivalence of settling grains, SEPM
947 Journal of Sedimentary Research Vol. 67 (1997). doi:10.1306/
948 d42685bd-2b26-11d7-8648000102c1865d.
- 949 [40] E. D. Sneed, R. L. Folk, Pebbles in the lower colorado river,
950 texas a study in particle morphogenesis, The Journal of Geology
951 66 (1958) 114–150. URL: <http://www.jstor.org/stable/30058239>.
952 doi:10.2307/30058239.
- 953 [41] N. A. Riley, Projection sphericity, SEPM Journal
954 of Sedimentary Research Vol. 11 (1941). doi:10.1306/
955 d426910c-2b26-11d7-8648000102c1865d.
- 956 [42] E. P. Cox, A method of assigning numerical and percentage val-
957 ues to the degree of roundness of sand grains, Journal of Paleontol-
958 ogy 1 (1927) 179–183. URL: <http://www.jstor.org/stable/1298056>.
959 doi:10.2307/1298056.
- 960 [43] N. Ritter, J. Cooper, New resolution independent measures of circu-
961 larity, Journal of Mathematical Imaging and Vision 35 (2009) 117–127.
962 doi:10.1007/s10851-009-0158-x.
- 963 [44] M. Pons, H. Vivier, K. Belaroui, B. Bernard-Michel, F. Cordier,
964 D. Oulhana, J. Dodds, Particle morphology: from visualisation to
965 measurement, Powder Technology 103 (1999) 44–57. doi:10.1016/
966 s0032-5910(99)00023-6.

- 967 [45] R. Ditscherlein, T. Leißner, U. A. Peuker, Preparation techniques for
968 micron-sized particulate samples in x-ray microtomography, *Powder*
969 *Technology* 360 (2020) 989–997. doi:10.1016/j.powtec.2019.06.001.
- 970 [46] R. Ditscherlein, T. Leißner, U. A. Peuker, Self-constructed automated
971 syringe for preparation of micron-sized particulate samples in x-ray
972 microtomography, *MethodsX* 7 (2020) 100757. doi:10.1016/j.mex.
973 2019.11.030.
- 974 [47] W. E. Lorensen, H. E. Cline, Marching cubes: A high resolution 3d
975 surface construction algorithm, in: *Proceedings of the 14th annual*
976 *conference on Computer graphics and interactive techniques, SIG-*
977 *GRAPH '87*, ACM, 1987, pp. 163–169. doi:10.1145/37401.37422.
- 978 [48] T. Lewiner, H. Lopes, A. W. Vieira, G. Tavares, Efficient implementa-
979 tion of marching cubes' cases with topological guarantees, *Journal of*
980 *Graphics Tools* 8 (2003) 1–15. doi:10.1080/10867651.2003.10487582.
- 981 [49] J. Lindblad, I. Nyström, *Surface Area Estimation of Digitized 3D Ob-*
982 *jects Using Local Computations*, Springer Berlin Heidelberg, 2002, pp.
983 267–278. doi:10.1007/3-540-45986-3_24.
- 984 [50] V. C. Janoo, Quantification of Shape, Angularity, and Surface texture
985 of Base Course Materials, Special report 98-1, Cold Regions Research
986 and Engineering Laboratory (U.S.), 1998. URL: [https://rosap.ntl.](https://rosap.ntl.bts.gov/view/dot/14065)
987 [bts.gov/view/dot/14065](https://rosap.ntl.bts.gov/view/dot/14065).
- 988 [51] V. Angelidakis, S. Nadimi, S. Utili, Elongation, flatness and compact-
989 ness indices to characterise particle form, *Powder Technology* 396
990 (2022) 689–695. doi:10.1016/j.powtec.2021.11.027.
- 991 [52] International Organization for Standardization, *Particle size analy-*
992 *sis—image analysis methods—part 1: Static image analysis methods*
993 (ISO 13322-1:2014), Standard, 2014.
- 994 [53] Dawson-Haggerty et al., *trimesh*, 2024. URL: <https://trimesh.org/>.
- 995 [54] S. Gillies, C. van der Wel, J. Van den Bossche, M. W. Taves, J. Arnott,
996 B. C. Ward, et al., *Shapely*, 2024. doi:10.5281/ZENODO.5597138.

- 997 [55] International Organization for Standardization, Particle size analy-
998 sis—image analysis methods—part 2: Dynamic image analysis meth-
999 ods (ISO 13322-2:2021), Standard, 2021.
- 1000 [56] V. Vouk, Projected area of convex bodies, *Nature* 162 (1948) 330–331.
1001 doi:10.1038/162330a0.
- 1002 [57] B. Meltzer, Shadow area of convex bodies, *Nature* 163 (1949) 220–220.
1003 doi:10.1038/163220b0.
- 1004 [58] J. R. Grace, A. Ebneyamini, Connecting particle sphericity and circu-
1005 larity, *Particuology* 54 (2021) 1–4. doi:10.1016/j.partic.2020.09.
1006 006.
- 1007 [59] L. Li, M. Iskander, Comparison of 2d and 3d dynamic image analysis
1008 for characterization of natural sands, *Engineering Geology* 290 (2021)
1009 106052. doi:10.1016/j.enggeo.2021.106052.